Elsevier Editorial System(tm) for Lithos
Manuscript Draft

Manuscript Number: LITHOS8034R2

Title: High pressure melting of eclogites and metasomatism of garnet peridotites from Monte Duria Area (Central Alps, N Italy): a proxy for melt-rock reaction during subduction

Article Type: Regular Article

Keywords: Slab melting; websterite; subduction fluids; dolomite; Adula nappe

Corresponding Author: Dr. Nadia Malaspina,

Corresponding Author's Institution: Università degli Studi di Milano Bicocca

First Author: Luca Pellegrino

Order of Authors: Luca Pellegrino; Nadia Malaspina; Stefano Zanchetta; Antonio Langone; Simone Tumiati

Abstract: In the Monte Duria area (Adula-Cima Lunga unit, Central Alps, N Italy) garnet peridotites occur in direct contact with migmatised orthogneiss (Mt. Duria) and eclogites (Borgo). Both eclogites and ultramafic rocks share a common high pressure (HP) peak at 2.8 GPa and 750 °C and post-peak static equilibration at 0.8-1.0 GPa and 850 °C. Garnet peridotites show abundant amphibole, dolomite, phlogopite and orthopyroxene after olivine, suggesting that they experienced metasomatism by crust-derived agents enriched in SiO_2, K_2O, CO_2 and H_2O. Peridotites also display LREE fractionation (La/Nd = 2.4) related to LREE-rich amphibole and clinopyroxene grown in equilibrium with garnet, indicating that metasomatism occurred at HP conditions. At Borgo, retrogressed garnet peridotites show low strain domains characterised by garnet compositional layering, cut by a subsequent low-pressure (LP) chlorite foliation, in direct contact with migmatised eclogites. Kfs+Pl+Qz+Cpx interstitial pocket aggregates and Cpx+Kfs thin films around symplectites after omphacite parallel to the Zo+Omp+Grt foliation in the eclogites suggest that they underwent partial melting at HP.
The contact between garnet peridotites and eclogites is marked by a tremolitite layer. The same rock also occurs as layers within the peridotite lens, showing a boudinage parallel to the garnet layering of peridotites, flowing in the boudin necks. This clearly indicates that the tremolitite boudins formed when peridotites were in the garnet stability field. Tremolitites also show Phl+Tc+Chl+Tr pseudomorphs after garnet, both crystallised in a static regime postdating the boudins formation, suggesting that they derive from a garnet-bearing precursor. Tremolitites have Mg# > 0.90 and Al_2O_3 = 2.75 wt.% pointing to ultramafic compositions but also show enrichments in SiO_2, CaO, and LREE suggesting that they formed after the reaction between the eclogite-derived melt and the garnet peridotite at HP. To test this hypothesis, we performed a thermodynamic modelling at fixed P = 3 GPa and T = 750 °C to model the chemical interaction between the garnet peridotite and the eclogite-derived melt. Our results show that this interaction produces an Opx+Cpx+Grt assemblage plus Amp+Phl, depending on the water activity in

the melt, suggesting that tremolitites likely derive from a previous garnet websterite with amphibole and phlogopite.

Both peridotites and tremolitites also show a selective enrichment in LILE recorded by amphiboles in the spinel stability field, indicating that a fluid-assisted metasomatic event occurred at LP conditions, leading to the formation of a chlorite foliation post-dating the garnet layering in peridotites, and the retrogression of Grt-websterites in tremolitites.

The Monte Duria area is a unique terrane where we can observe syn-deformation eclogite-derived melt interacting with garnet peridotite at HP, proxy of subduction environments.

Research Data Related to this Submission

There are no linked research data sets for this submission. The following reason is given:
Data will be made available on request

High pressure melting of eclogite and metasomatism of garnet peridotites from Monte Duria Area (Central Alps, N Italy): a proxy for melt-rock reaction during subduction

Luca Pellegrino[1], Nadia Malaspina[1*], Stefano Zanchetta[1], Antonio Langone[2], Simone Tumiati[3]

[1*] Dipartimento di Scienze dell'Ambiente e della Terra, Università degli Studi di Milano-Bicocca, Piazza della Scienza 4, 20126 Milano, Italy (nadia.malaspina@unimib.it; ph:+39 0264482042; fax: +39 0264482073)

[2] Istituto di Geoscienze e Georisorse-C.N.R. U.O.S. of Pavia, Via Ferrata 1, 27100 Pavia, Italy

[3] Dipartimento di Scienze della Terra, Università degli Studi di Milano, via Mangiagalli 34, 20133 Milano, Italy

Abstract

In the Monte Duria area (Adula-Cima Lunga unit, Central Alps, N Italy) garnet peridotites occur in direct contact with migmatised orthogneiss (Mt. Duria) and eclogites (Borgo). Both eclogites and ultramafic rocks share a common high pressure (HP) peak at 2.8 GPa and 750 °C and post-peak static equilibration at 0.8-1.0 GPa and 850 °C. Garnet peridotites show abundant amphibole, dolomite, phlogopite and orthopyroxene after olivine, suggesting that they experienced metasomatism by crust-derived agents enriched in SiO_2, K_2O, CO_2 and H_2O. Peridotites also display LREE fractionation (La/Nd = 2.4) related to LREE-rich amphibole and clinopyroxene grown in equilibrium with garnet, indicating that metasomatism occurred at HP conditions. At Borgo, retrogressed garnet peridotites show low strain domains characterised by garnet compositional layering, cut by a subsequent low-pressure (LP) chlorite foliation, in direct contact with migmatised eclogites. Kfs+Pl+Qz+Cpx interstitial pocket aggregates and Cpx+Kfs thin films

around symplectites after omphacite parallel to the Zo+Omp+Grt foliation in the eclogites suggest that they underwent partial melting at HP.

The contact between garnet peridotites and eclogites is marked by a tremolitite layer. The same rock also occurs as layers within the peridotite lens, showing a boudinage parallel to the garnet layering of peridotites, flowing in the boudin necks. This clearly indicates that the tremolitite boudins formed when peridotites were in the garnet stability field. Tremolitites also show Phl+Tc+Chl+Tr pseudomorphs after garnet, both crystallised in a static regime postdating the boudins formation, suggesting that they derive from a garnet-bearing precursor. Tremolitites have Mg# > 0.90 and Al_2O_3 = 2.75 wt.% pointing to ultramafic compositions but also show enrichments in SiO_2, CaO, and LREE suggesting that they formed after the reaction between the eclogite-derived melt and the garnet peridotite at HP. To test this hypothesis, we performed a thermodynamic modelling at fixed P = 3 GPa and T = 750 °C to model the chemical interaction between the garnet peridotite and the eclogite-derived melt. Our results show that this interaction produces an Opx+Cpx+Grt assemblage plus Amp+Phl, depending on the water activity in the melt, suggesting that tremolitites likely derive from a previous garnet websterite with amphibole and phlogopite.

Both peridotites and tremolitites also show a selective enrichment in LILE recorded by amphiboles in the spinel stability field, indicating that a fluid-assisted metasomatic event occurred at LP conditions, leading to the formation of a chlorite foliation post-dating the garnet layering in peridotites, and the retrogression of Grt-websterites in tremolitites.

The Monte Duria area is a unique tarrane where we can observe syn-deformation eclogite-derived melt interacting with garnet peridotite at HP, proxy of subduction environments.

*Highlights (for review)

High pressure melting of eclogite and metasomatism of garnet peridotites from Monte Duria Area (Central Alps, N Italy): a proxy for melt-rock reaction during subduction

Luca Pellegrino[1], Nadia Malaspina[1*], Stefano Zanchetta[1], Antonio Langone[2], Simone Tumiati[3]

[1*] Dipartimento di Scienze dell'Ambiente e della Terra, Università degli Studi di Milano-Bicocca, Piazza della Scienza 4, 20126 Milano, Italy (nadia.malaspina@unimib.it; ph:+39 0264482042; fax: +39 0264482073)

[2] Istituto di Geoscienze e Georisorse-C.N.R. U.O.S. of Pavia, Via Ferrata 1, 27100 Pavia, Italy

[3] Dipartimento di Scienze della Terra, Università degli Studi di Milano, via Mangiagalli 34, 20133 Milano, Italy

Highlights

- Structural and microstructural evidence of eclogite partial melting at P-T conditions corresponding to warm subduction.
- Unique case study of eclogite-derived melts interacting with garnet peridotite at high pressure in the Alps (Adula-Cima Lunga unit, N Italy).
- Syn-deformation development of garnet websterites during melt-peridotite interaction in subduction environments.

High pressure melting of eclogite and metasomatism of garnet peridotites from Monte Duria Area (Central Alps, N Italy): a proxy for melt-rock reaction during subduction

Luca Pellegrino[1], Nadia Malaspina[1*], Stefano Zanchetta[1], Antonio Langone[2], Simone Tumiati[3]

[1*] Dipartimento di Scienze dell'Ambiente e della Terra, Università degli Studi di Milano-Bicocca, Piazza della Scienza 4, 20126 Milano, Italy (nadia.malaspina@unimib.it; ph:+39 0264482042; fax: +39 0264482073)

[2] Istituto di Geoscienze e Georisorse-C.N.R. U.O.S. of Pavia, Via Ferrata 1, 27100 Pavia, Italy

[3] Dipartimento di Scienze della Terra, Università degli Studi di Milano, via Mangiagalli 34, 20133 Milano, Italy

Highlights

- Structural and microstructural evidence of eclogite partial melting at P-T conditions corresponding to warm subduction.
- Unique case study of eclogite-derived melts interacting with garnet peridotite at high pressure in the Alps (Adula-Cima Lunga unit, N Italy).
- Syn-deformation development of garnet websterites during melt-peridotite interaction in subduction environments.

Abstract

In the Monte Duria area (Adula-Cima Lunga unit, Central Alps, N Italy) garnet peridotites occur in direct contact with migmatised orthogneiss (Mt. Duria) and eclogites (Borgo). Both eclogites and ultramafic rocks share a common high pressure (HP) peak at 2.8 GPa and 750 °C and post-peak static equilibration at 0.8-1.0 GPa and 850 °C. Garnet peridotites show abundant amphibole,

dolomite, phlogopite and orthopyroxene after olivine, suggesting that they experienced metasomatism by crust-derived agents enriched in SiO_2, K_2O, CO_2 and H_2O. Peridotites also display LREE fractionation (La/Nd = 2.4) related to LREE-rich amphibole and clinopyroxene grown in equilibrium with garnet, indicating that metasomatism occurred at HP conditions. At Borgo, retrogressed garnet peridotites show low strain domains characterised by garnet compositional layering, cut by a subsequent low-pressure (LP) chlorite foliation, in direct contact with migmatised eclogites. Kfs+Pl+Qz+Cpx interstitial pocket aggregates and Cpx+Kfs thin films around symplectites after omphacite parallel to the Zo+Omp+Grt foliation in the eclogites suggest that they underwent partial melting at HP.

The contact between garnet peridotites and eclogites is marked by a tremolitite layer. The same rock also occurs as layers within the peridotite lens, showing a boudinage parallel to the garnet layering of peridotites, flowing in the boudin necks. This clearly indicates that the tremolitite boudins formed when peridotites were in the garnet stability field. Tremolitites also show Phl+Tc+Chl+Tr pseudomorphs after garnet, both crystallised in a static regime postdating the boudins formation, suggesting that they derive from a garnet-bearing precursor. Tremolitites have Mg# > 0.90 and Al_2O_3 = 2.75 wt.% pointing to ultramafic compositions but also show enrichments in SiO_2, CaO, and LREE suggesting that they formed after the reaction between the eclogite-derived melt and the garnet peridotite at HP. To test this hypothesis, we performed a thermodynamic modelling at fixed P = 3 GPa and T = 750 °C to model the chemical interaction between the garnet peridotite and the eclogite-derived melt. Our results show that this interaction produces an Opx+Cpx+Grt assemblage plus Amp+Phl, depending on the water activity in the melt, suggesting that tremolitites likely derive from a previous garnet websterite with amphibole and phlogopite.

Both peridotites and tremolitites also show a selective enrichment in LILE recorded by amphiboles in the spinel stability field, indicating that a fluid-assisted metasomatic event occurred at LP

conditions, leading to the formation of a chlorite foliation post-dating the garnet layering in peridotites, and the retrogression of Grt-websterites in tremolitites.
The Monte Duria area is a unique terrane where we can observe syn-deformation eclogite-derived melt interacting with garnet peridotite at HP, proxy of subduction environments.

Keywords

Slab melting, websterite, subduction fluids, dolomite, Adula nappe.

1. Introduction

The partial melting of metasedimentary and metagranitic rocks interacting with garnet peridotites – proxy of the interaction between the subducted crust and the overlying mantle – can be found in high-ultrahigh pressure (HP-UHP) terranes such as Ulten Zone in the Central Italian Alps (Rampone and Morten, 2001; Tumiati et al., 2003; Scambelluri et al., 2006) and the chinese Dabie-Sulu belt (Malaspina et al., 2006; 2009). Alternatively, evidence of partial melting of HP rocks representative of the mafic portions of the subducted slab is very rare and its evidence is seen in the production of peraluminous trondhjemite–tonalite melts (so-called adakites) forming volcanic suites of andesitic to rhyodacitic composition (Drummond et al., 1996). The observation of HP partial melting of eclogites has been reported only by Wang et al. (2014) in the Central Sulu orogen, while to date the direct interaction between eclogite-derived melts and peridotites at HP has never been observed *in situ* in orogenic peridotites.

Melting of mafic rocks in a subducting lithosphere at HP requires at least T = 750 °C at P = 3 GPa, under H_2O saturated conditions (Schmidt and Poli, 2014), typical of low angle subduction systems (Peacock and Wang, 1999) also called “warm subduction” (Syracuse et al., 2010). The Monte Duria area (Adula-Cima Lunga nappe, Central Alps, Italy) is a unique terrane where we can observe eclogite-derived melt interacting with garnet peridotite at P-T conditions proxy of “warm” subduction paths. In this area garnet peridotites occur in direct contact with migmatised orthogneiss and eclogites, sharing a common metamorphic history reaching HP peak at 2.8 GPa and 750 °C and post-peak static equilibration at 0.8-1 GPa and 850 °C (Tumiati et al., 2018). In this study we will show that garnet peridotites from the Monte Duria area record a multistage metasomatic event by eclogite-derived adakite-like melts at HP inducing a selective enrichment in LREE, and by retrograde fluids at lower pressures yielding to LILE enrichments in amphiboles. The interaction between garnet peridotites and eclogite leucosomes also produces a modal metasomatism evidenced by the occurrence of garnet websterite layers at the contact between eclogite and peridotite, now retrogressed in the tremolite stability field.

The fate of crust-derived melts in the associated peridotites and their capability to transport crustal components to the mantle is still matter of debate. Many occurrences show that crustal melts may migrate into the mantle by porous flow, producing almost monomineralic metasomatic orthopyroxene and phlogopite layers at the slab-mantle interface (e.g. Malaspina et al., 2006; 2009; Endo et al., 2015). Such a mechanism, however, may limit the crust-to-mantle mass transfer unless they are partitioned into residual aqueous fluids (Malaspina et al., 2009). Alternatively, metasomatic melts may migrate into the mantle by focussed flow, forming a network of pyroxenite veins as shown by metasomatised mantle xenoliths from arc lavas (e.g. Arai et al., 2003; Kepezhinskas et al., 1995). We will show that the melt-peridotite interaction preserved in Borgo outcrop of Monte Duria area occurred under a deformation regime (shearing) at HP, promoting the combination of porous and focussed flow of eclogite-derived melts into the garnet peridotite. The melt-enhanced deformation and flow in garnet peridotites documented in the Monte Duria area may represent an exhumed example of crustal flow channels forming at the slab-mantle interface, that facilitate the migration of crustal melts in the supra-subduction mantle.

2. Geological and petrological background

The Adula-Cima Lunga nappe (ACL) complex is the structurally highest unit of the Sub-Penninic domain occurring within the Lepontine Dome (Milnes, 1974; Schmid et al., 1996). In this area of the Central Alps, the ACL is comprised between the underlying Lower Penninic Simano and Leventina nappes (Fig. 1) and the Middle Penninic units of Tambò, Suretta and Schams nappes (Schmid et al., 1990). The base of the ACL is defined by the Misox Zone, a N-S trending heterogeneous unit made by carbonatic and siliciclastic metasediments (Bündnerschiefer *Auct.*), by MORB-derived amphibolites and slivers of continental basement (Stucki et al., 2003). The southern limit of the ACL (Fig. 1) is represented by the Paina Fault (Fumasoli, 1974), marked in the field by a thin slice of silicate-bearing marble interpreted to represent the upper contact of the ACL (Fumasoli, 1974; Schmid et al., 1996). The Bellinzona-Dascio zone, occurring south of the Paina Fault (Fig. 1), is either considered to be the continuation of the Misox Zone (Schmid et al., 1996), or as to be part of the ACL (Berger et al., 2005). At the SE boundary of ACL the Gruf Complex is separated from the ACL unit by the Forcola normal fault. The Gruf complex experienced ultrahigh temperature (UHT) metamorphism and is considered to be of Permian (Galli et al., 2011) or Oligocene age (Droop and Bucher, 1984; Liati and Gebauer, 2003; Nicollet et al., 2018).

The ACL mainly consists of ortho- and paragneiss of pre-Mesozoic age, partially retrogressed eclogites, amphibolites, marbles, metasedimentary rocks of supposed Mesozoic origin (Galster et al., 2012) and minor serpentinite and peridotite bodies (Evans and Trommsdorff, 1978; Fumasoli, 1974; Heinrich, 1986). The ACL experienced high pressure (HP) metamorphism during both the Variscan (e.g. Biino et al., 1997; Herwartz et al., 2011; Liati et al., 2009) and the Alpine orogenic cycle (Dale and Holland, 2003; Meyre and Frey, 1998; Nagel et al., 2002). Despite the intensive Alpine metamorphism and deformation, relicts of pre-Alpine (Variscan) HP metamorphism are still preserved in the central and northern sectors of the ACL (Herwartz et al., 2011; Liati et al., 2009). P-T estimates of HP assemblage in eclogites from Confin, Val Large and Trescolmen, suggest equilibrium conditions of P = 1.4-2.2 GPa and T = 500-700 °C (Dale and Holland, 2003; Nagel, 2008). Peak conditions for the Alpine eclogites increase southward from P ≈ 2.0 GPa and T = 600 °C in the north, to P ≈ 3.0 GPa and T = 650-750 °C in the south (Brouwer et al., 2005; Dale and Holland, 2003; Heinrich, 1986). The highest eclogitic peak conditions were recognised in the ultramafic rocks cropping out in the southern part of the nappe.

In the ACL garnet peridotites occur at three localities, from west to east: Cima di Gagnone (Evans and Trommsdorff, 1978); Alpe Arami (Mockel, 1969); and Monte Duria (Fumasoli, 1974). Chlorite harzburgite and garnet lherzolites from Cima di Gagnone represent slivers of subcontinental mantle exposed at the seafloor during the formation of the Alpine Tethys and subsequently involved in the Alpine subduction cycle (Evans and Trommsdorff, 1978; Trommsdorff et al., 2000; Scambelluri et al., 2014). Thermobarometry of the peak garnet-facies assemblage provided estimates of 750-800 °C and 2.5-3 GPa for the eclogitic event (Evans & Trommsdorff, 1978; Nimis and Trommsdorff, 2001). Garnet peridotites from Alpe Arami have been interpreted as derived either from a subducted sub-continental lithospheric mantle (Trommsdorff et al., 2000) or from portions of supra-subduction mantle (Brenker and Brey, 1997). Similarly, garnet and chlorite peridotites from Monte Duria Area have been interpreted as supra-subduction mantle peridotites located above the subducting Alpine Tethys lithosphere during late Cenozoic (Hermann et al., 2006). P-T estimates for the HP metamorphism experienced by garnet peridotites of Alpe Arami and Monte Duria yielded P-T conditions of 3.2 GPa and 844 °C and 3.0 and 830 °C, respectively (Nimis and Trommsdorff, 2001). Similar peak pressure conditions and slightly lower temperature (2.8 ± 0.2 GPa and 730 ± 20 °C) have been reported by Tumiati et al. (2018) for the HP assemblages of garnet peridotites and associated eclogites of Monte Duria area.

Recently Tumiati et al. (2018) provided also evidence for a previously unknown LP-(U)HT metamorphic event which post-dates the HP assemblages and pre-dates the Barrovian metamorphism of the Lepontine Dome in peridotites and eclogites of Monte Duria area. Pressure-temperature estimates of LP-(U)HT assemblages found in both mafic and ultramafic rocks yielded T = 850 °C and P = 0.8-1.2 GPa. It is worthy of note that similar conditions are also reported for the

UHT stage recorded in the sapphirine-bearing granulites and charnockites of the near Gruf Complex (Galli et al., 2011).

The peridotites and associated crustal rocks of the Monte Duria area, together with the whole ACL complex, eventually experienced the post-collisional metamorphism that affected the entire central Alpine nappe stack (Nagel, 2008). The Barrovian-type metamorphism increases southward from upper green-schists facies in the north, to high amphibolite facies in the south (Nagel, 2008; Todd and Engi, 1997), where it promoted crustal anatexis in a narrow belt close to the Insubric Line (e.g. Burri et al., 2005; Rubatto et al., 2009). Partial melting was promoted by fluid infiltration and occurred between 32 and 22 Ma suggesting a protracted high thermal history during Barrovian-type metamorphism (Rubatto et al., 2009).

3. Field occurrence

The Monte Duria area is located at northwest of the Como Lake (Northern Italy) (Fig. 1a) and it is part of the southern ACL. Peridotite lenses hosted by crustal rocks occur at two localities: (i) Mt. Duria and (ii) Borgo (Fig. 1b). At Mt. Duria garnet peridotites are hosted by migmatitic biotite-muscovite gneiss whereas at Borgo a large chlorite peridotite body is in direct contact with amphibole-bearing migmatites, the latter containing several boudins of lithologically heterogeneous eclogites (Tumiati et al., 2018; Fig. 2).

At the mesoscale, the garnet peridotites of Mt. Duria display a compositional layering consisting of garnet-rich and garnet-poor layers, transposed by a chlorite foliation. Such foliation becomes more penetrative close to the outermost part of the peridotite lenses (Fig. 3a, b). Peridotites consist of garnet, clinopyroxene and minor amphibole porphyroclasts enclosed in a dark fine-gained matrix consisting of olivine, clinopyroxene and orthopyroxene. Garnet is surrounded by kelyphitic coronas and in most of the peridotite lenses is progressively replaced by chlorite pseudomorphs. Garnet-pyroxenite lenses often occur within the garnet peridotite bodies of the Monte Duria area (Fumasoli, 1974; Hermann et al., 2006).

At Borgo, an hm-sized chlorite peridotite body is in direct contact with amphibole-bearing migmatites containing boudins of mafic, high-Al_2O_3 and kyanite-bearing eclogites (Fig. 2; Tumiati et al., 2018). The chlorite peridotite body, along with the associated mafic rocks, is enclosed within biotite-bearing migmatitic gneiss (yellow in Fig. 2). The chlorite peridotite (lilac in Fig. 2) mainly consists of fine-grained olivine, orthopyroxene and rare clinopyroxene. Garnet is always replaced by chlorite pseudomorphs (Fig. 3c), likely indicating that the Borgo chlorite peridotites represent the retrogressed variety of the garnet peridotites of Mt. Duria. Chlorite peridotites preserve a compositional layering made by alternate levels rich or poor in chlorite pseudomorphs after garnet. Such layering is locally transposed by a new chlorite-bearing foliation (Fig. 3c, d).

The contact between the peridotite body and the associated mafic rocks at Borgo is marked by the occurrence of a tremolitite layer (violet in Fig. 2) composed by more than 90 vol.% of fine-grained tremolite associated with several phlogopite + chlorite + talc + tremolite pseudomorphs after garnet and minor Mg-hornblende. These rocks also occur as m-scale boudins within the peridotite body and show sharp contacts with the host peridotite (Fig. 4a, b, c). The garnet foliation in the peridotite body wraps around the boudins and flows into the boudins necks indicating that the deformation of tremolitite precusors occurred during the development of the garnet foliation in the host peridotite (Fig. 4b, c). Such boudins are confined within 20 meters from the contact (Fig. 2).

The amphibole-bearing migmatites of Borgo display evidence for partial melting at different scales. These rocks (salmon in Fig. 2) display mm- to m-thick leucosomes consisting of quartz + plagioclase + K-feldspar + biotite and amphibole-rich restitic layers (Fig. 4d). Partial melting occurred in a deformation regime, as displayed by the strong layered structure of amphibole-bearing migmatites and the occurrence of peculiar deformation structures like lobes and cusps (Fig. 4e; McLellan, 1989). These migmatites contain boudins of mafic, high-Al_2O_3 and kyanite-bearing eclogites (Tumiati et al., 2018). Fine grained, dark green mafic eclogites (dark green in Fig. 2) occur as m-sized boudins. These rocks show a compositional layering consisting of garnet-rich and garnet-poor layers. At the rim of the boudins, such layering is crosscut by the foliation of the surrounding amphibole-bearing migmatites. Larger boudins (up to 10 meters) of light green, kyanite-bearing eclogites also occur (Fig. 2). As already described for the mafic eclogites, a compositional layering marked by garnet-rich and garnet-poor layers represents the main fabric at the mesoscale. The high-Al_2O_3 eclogite (red rim in Fig. 2) occurs as a cm-thick reddish corundum-rich rim at the contact between kyanite-bearing eclogite and amphibole-bearing migmatites. These rocks are garnet-free and the only HP relicts are porphyroblastic kyanite and emerald-green zoisite (Tumiati et al., 2018).

The peridotite body and the associated mafic rocks are both separated from the surrounding migmatitic biotite gneiss by a few meters thick mylonitic shear zone (Fig. 2; Fig. S-1a). The migmatitic gneiss has a stromatic structure defined by alternating leucocratic bands composed by quartz, plagioclase and alkali feldspar, and melanocratic domains enriched in biotite.

4. Petrography

Representative samples among garnet peridotites from Mt. Duria and chlorite peridotites, tremolitites, mafic eclogite, kyanite-bearing eclogite, high-Al_2O_3 eclogite and amphibole-bearing migmatites from Borgo (Fig. 2) have been selected for this study. All the recognised mineral assemblages and the relative metamorphic conditions are summarized in Table 1.

4.1. Peridotites

Garnet peridotites from Mt. Duria show porphyroclastic texture with mm-sized garnet, clinopyroxene (Cpx_1), orthopyroxene (Opx_1) and amphibole (Amp_1), surrounded by fine-grained recrystallised matrix of olivine, orthopyroxene (Opx_2), clinopyroxene (Cpx_2), amphibole (Amp_2)

and Cr-spinel (Fig. 5a, b). Garnet porphyroclasts contain inclusions of clinopyroxene, orthopyroxene and olivine. In sample B3A inclusions of edenitic to pargasitic amphibole and dolomite have been observed in Cpx_1. Frequently, garnet is statically replaced by chlorite (Chl_1)-bearing pseudomorphs surrounded by amphibole + spinel coronas (Fig. S-2a). During the subsequent LP-(U)HT metamorphism (see Tumiati et al., 2018), Chl_1 decomposes into a orthopyroxene + spinel assemblage (Fig. S-2b, c), while composite kelyphitic coronas consisting of orthopyroxene (Opx_{Sym}) after olivine and orthopyroxene (Opx_{Sym}) + clinopyroxene (Cpx_{Sym}) + spinel (Sp_{Sym}) ± amphibole (Amp_{Sym}) after garnet developed in correspondence of the previous garnet-olivine grain boundaries. In kelyphites replacing olivine tiny crystals of baddeleyite and srilankite occur, while sapphirine crystallises within symplectitic assemblages around garnet (Tumiati et al., 2018).

Chlorite peridotites display a porphyroclastic microstructure with mm-sized chloritised garnet, in textural equilibrium with coarse olivine, orthopyroxene and minor clinopyroxene. Sample C2A shows a finer-grained assemblage made of olivine, clinopyroxene, orthopyroxene, amphibole (Amp_2) and Cr-spinel, resembling the recrystallised matrix of garnet peridotite from Mt. Duria. Both samples C2A and DB113 display a strong foliation defined by syn-tectonic chlorite (Chl_3) and amphibole (Amp_3), post-dating the porphyroclastic and neoblastic assemblages (Fig. S-2b). Notably, sample DB113 has been collected close to the contact with the innermost tremolitite boudins and shows relict olivine and orthopyroxene extensively statically overgrown by a new generation of porphyroblastic orthopyroxene (Opx_{Porph}), Mg-hornblende (Amp_{Porph}) and phlogopite (Phl_{Porph}) (Fig. 5c). These microstructures clearly indicate a metasomatic event pre-dating the chlorite foliation. Several dolomite crystals (Fig. 5d) and round-shaped brucite + calcite pseudomorphs after dolomite also occur within the olivine matrix.

4.2 Tremolitite layers within the peridotite

Tremolitites display an assemblage dominated by tremolite, Mg-hornblende and minor chlorite. In all the investigated samples (DB148, DB151 and DB179), tremolite forms a mosaic-like texture with 120° triple junctions and straight grain boundaries. The tremolite matrix hosts older mm-sized Mg-hornblende porphyroblasts (Fig. 5e). Mg-hornblende is zoned, showing dusty cores with opaque minerals occurring along the cleavages, and clear inclusion-free rims. Isolated phlogopite (Phl_3) + chlorite (Chl_3) + talc + tremolite hexagonal pseudomorphs after garnet have been recognised in textural equilibrium with tremolite (Fig. 5f).

4.3 Eclogite boudins and amphibole-bearing migmatites

Mafic eclogites display a porphyroblastic microstructure with mm-sized garnet, K-feldspar, quartz and zoisite embedded in a fine-grained matrix composed by Mg-hornblende (Amp_2), diopside-rich clinopyroxene (Cpx_2) and albitic plagioclase (Pl_2) (Fig. 6a). Garnet is usually zoned, showing dusty cores with inclusions of quartz, omphacite and minor rutile, and inclusions free rims. A 30-μm inclusion of dolomite has been also observed. Garnet is occasionally replaced by pseudomorphs composed by Mg-hornblende (Amp_2) and plagioclase (Pl_2). K-feldspar locally displays 50-100-μm thick clinopyroxene ± Mg-hornblende coronas (Fig. 6a). Few quartz porphyroblasts have irregular shape, with locally lobate-cuspate grain boundaries surrounded by 50-μm thick coronas composed by K-feldspar (Kfs_M) and minor clinopyroxene (Cpx_M) (Fig. 6a). Zoisite commonly occurs as 100-150-μm porphyroblasts and locally surrounded by tiny, ameboid allanite crystals (Fig. 6b).

Kyanite-bearing eclogites display a porphyroblastic microstructure with abundant garnet, kyanite and quartz. Few tiny inclusions of omphacite and rutile occur within garnet and kyanite porphyroblasts. The rock matrix is composed by Mg-hornblende (Amp_2), diopside-rich clinopyroxene (Cpx_2) and albitic plagioclase (Pl_2). Similarly to the mafic eclogites, garnet and kyanite are usually replaced by symplectitic intergrowths consisting of Mg-hornblende (Amp_{Sym})

and albitic plagioclase (Pl_{Sym}), whereas symplectites around kyanite are composed by anorthitic plagioclase (Pl_{Sym}), spinel (Sp_{Sym}), orthopyroxene (Opx_{Sym}) and minor sapphirine (c.f. Tumiati et al., 2018).

The high-Al_2O_3 eclogites display a strong foliation defined by syn-tectonic porphyroblastic kyanite in textural equilibrium with quartz and zoisite porphyroblasts. Also these minerals are embedded in a fine-grained matrix composed by diopside-rich clinopyroxene (Cpx_2) + albite-rich plagioclase (Pl_2) + Mg-hornblende (Amp_2) pseudomorphs after omphacite. Kyanite is partly replaced by symplectitic coronas consisting of An-rich plagioclase (Pl_{Sym}), spinel (Sp_{Sym}), corundum and minor sapphirine (c.f. Tumiati et al., 2018). Similarly to K-feldspar in mafic eclogites, also quartz in these samples locally displays corroded edges surrounded by fine-grained intergrowths consisting of anhedral K-feldspar (Kfs_M) and clinopyroxene (Cpx_M) (Fig. 6c). The Cpx_M + Kfs_M intergrowths are preferentially oriented parallel to the main foliation suggesting that they formed in a deformation regime when the kyanite + omphacite + quartz HP assemblage was still stable. Interstitial pocket aggregates made of Kfs_M + Cpx_M + plagioclase (Pl_M)+ quartz (Qz_M) have been also observed at quartz grain boundaries (Fig. 6d). In all the three types of eclogites, the symplectitic domains are surrounded by coronas defined by porphyroblastic pargasitic hornblende (Amp_3) and biotite.

The amphibole-bearing migmatites hosting the eclogite boudins display a layered microstructure, consisting of leucocratic domains composed by quartz + plagioclase ± Mg-hornblende ± biotite and melanocratic domains enriched in hornblende. Leucocratic domains display a mosaic-like equilibrium microtexture with grain boundaries triple junctions at 120°. The melanocratic domains are strongly foliated dominated by Mg-hornblende and by a fine-grained matrix consisting of clinopyroxene (Cpx_2), amphibole (Amp_2) and albitic plagioclase (Pl_2) replacing previous garnet and omphacite (Fig. 6e, f). These microtextures indicate that the hornblende-rich domains derive from a previous eclogitic precursor.

5. Bulk rock chemistry

5.1. Major elements

The major elements composition of the investigated rocks is reported in Table 2. As shown in Figure 7, the composition of Mt. Duria garnet peridotites resembles that of the reference Depleted Mantle (Salters and Stracke, 2004), displaying X_{Mg} = 0.90, Ni = 1960-1975 ppm, and low Al_2O_3 (2.67-3.05 wt.%) and CaO (2.16-2.52 wt.%) concentrations. In Figure 7 the composition of peridotites from other localities of the Central and Eastern Alps have been also portrayed. Our samples plot close to the Alpe Arami (AA), Bellinzona-Dascio Zone (BDZ) and Ulten (UZ) peridotites, whereas the ultramafic rocks from Cima di Gagnone (CdG) show lower Ni (1386-1614 ppm), and slightly higher Al_2O_3 (2.87-4.44 wt.%) and CaO (2.48-3.65 wt.%) concentrations. Tremolitites (purple square) show X_{Mg} = 0.91 and Al_2O_3 concentrations comparable to mantle values. Moreover, in the X_{Mg}-Ni variation diagram, tremolitites plot into the field of the ultramafic compositions probably indicating that they derive from an ultramafic precursor. Despite this mantle signature, they show high SiO_2 (up to ca. 55 wt.%), high CaO (12.38 wt.%) and low Ni (554 ppm) concentrations (Tab. 2).

The bulk-rock composition of mafic, kyanite-bearing and high-Al_2O_3 eclogites indicates that they all have a mafic composition (SiO_2 = 48.96-51.17 wt.%; Tab. 2, Figure 7) and are compared to that of N-MORB (Gale et al., 2013), layered mid ocean-ridge gabbros (Gillis et al., 2014) and ophiolitic gabbros from the Bellinzona-Dascio Zone (Stucki et al., 2003). The composition of the mafic eclogite overlaps that of the reference N-MORB showing X_{Mg} = 0.61, Ni = 139 ppm, CaO = 9.57 wt.% and Al_2O_3 = 15.50 wt.%. The other two types of eclogite display a composition resembling that of reference gabbros with X_{Mg} ranging from 0.74 to 0.83 and the highest CaO (11.52-11.67 wt.%) and Al_2O_3 (16.11-18.63 wt.%) concentrations.

5.2. Trace elements

The bulk rock trace elements composition of the analysed samples is reported in Table 2 and portrayed in Figure 8, normalised to the Primitive Mantle (PM, McDonough and Sun, 1995). The trace elements pattern of the Depleted Mantle (DM, Salters and Stracke, 2004) is also reported for comparison (DM, blue bold line of Fig. 8a, b). Garnet peridotites show absolute rare earth elements (REE) concentrations slightly lower than the PM, with fractionated patterns enriched in light-REE (LREE) (La_N/Nd_N = 2.4) relative to the medium-REE (MREE) and heavy-REE (HREE) (Fig. 8a). Also the trace elements composition of the studied peridotites is compared to that of peridotites from Cima di Gagnone and Ulten Zone (Fig. 8a, b). The studied peridotites overlap the fractionated REE patterns of Ulten peridotites, whereas Cima di Gagnone ultramafic rocks (grey area) display LREE depletion with respect to MREE and HREE following the same pattern of the DM. In terms of other trace elements, the composition of the investigated peridotites broadly resembles that of Ulten Zone and Cima di Gagnone ultramafic rocks, showing relatively high large ion lithophile elements (LILE) concentrations (i.e. Cs = 50×PM, Fig. 8b).

Tremolitites have REE concentrations up to 2.6×PM with enrichments in MREE and LREE (i.e. La_N/Er_N = 2.15 and Nd_N/Er_N = 2.97) relative to HREE (Fig. 8c). These rocks do not show any appreciable LILE enrichment except for relatively high Pb concentrations (up to 10×PM; Fig. 8d).

The trace elements compositions of eclogites are compared with the composition of N-MORB (dark grey line in Fig. 8e; Gale et al., 2013) and ophiolitic gabbros from Bellinzona-Dascio Zone (light grey field in Fig. 8e; Stucki et al., 2003). The REE pattern of mafic eclogite broadly resembles that of reference N-MORB with REE absolute concentrations up to10×PM and a slight Eu negative anomaly. Both high-Al_2O_3 and kyanite eclogites display REE concentrations almost one order of magnitude lower than those of mafic eclogites (Fig. 8e), showing a slight fractionation in LREE with respect to MREE and HREE (La/Nd_N = 1.24), falling in the patterns range of Bellinzona-Dascio Zone gabbros, except for the lack of a strong positive Eu anomaly. Only the high-Al_2O_3 eclogite shows a weak Eu positive anomaly, likely indicating that some cumulus plagioclase was present in the igneous protolith of these rocks. The whole-rock composition of eclogites also shows high LILE concentrations (i.e. Cs up to 90×PM), negative anomalies in Ba and Nb, positive anomalies in Sr (except for the mafic eclogite) and high U/Th ratio (Fig. 8f).

The Cpx_M + Kfs_M pocket aggregates around relict quartz and Pl_2+Cpx_2+Amp_2 symplectite after omphacite in high-Al_2O_3 eclogite D9 (Fig. 6c, S-3) have strongly fractionated REE patterns with enrichment in HREE relative to LREE (La_N/Er_N = 0.11), and a marked Eu negative anomaly (Fig. 8e). It also shows high LILE concentrations (Rb = 2645×PM), negative anomalies in Nb and Ti, and low U/Th = 1.5 (Fig. 8f). The inset of Figure 8e also portrays the REE pattern of allanite surrounding zoisite, which shows strong enrichment in LREE and HREE.

6. Mineral chemistry

6.1 Major elements

The major elements composition of the analysed rock forming minerals is reported in Table 3 and portrayed in Figures 9 and 10.

6.1.1. Peridotites

In garnet peridotites, olivine has forsteritic composition with X_{Mg} = 0.90, comparable to that of the bulk rock. Garnet is pyrope-rich ($Py_{67}Alm_{18}Gr_{15}$) with a core-to-rim increase of Al and Fe^{2+} ($Py_{64}Alm_{21}Gr_{15}$) and a complementary decrease of Mg (Tab. 3), likely related to a retrograde equilibration (Tab. 3). Clinopyroxenes have a diopside-rich composition (Tab. 3). In the Na-$Al^{(VI)}$ diagram (Fig. 9a) clinopyroxene of sample B3A displays a progressive decrease of Na and $Al^{(VI)}$ from Cpx_1, to neoblastic Cpx_2, to symplectitic Cpx_{Sym}. Cpx_1 of sample A2C2 displays a sharp zonation with a core-to-rim decrease of Na and $Al^{(VI)}$. The composition of the analysed rims approaches that of clinopyroxene in equilibrium with post-peak minerals (Cpx_2), in agreement with a retrograde equilibration of clinopyroxenes at lower pressure. Cpx_2 also shows Al-rich composition with Al up to 0.07 a.p.f.u. (Tab. 3). Old coarse orthopyroxenes (Opx_1) are enstatites with X_{Mg} = 0.91. In the Si-Al diagram (dark grey symbols in Fig. 9b) they display an increase of Al from Opx_1 in equilibrium with garnet to Opx_{Sym} observed in kelyphites, and a complementary decrease in Si, following the same retrogression equilibration recorded by garnet and clinopyroxene.

As shown in Figure 9c, Amp_1 and Amp_2 are pargasitic to edenitic in composition, while symplectitic amphiboles (Amp_{Sym}) vary from tschermakite to Mg-hornblende in sample A2C2, to pargasite in peridotite B3A (Tab. 3). In both Na-$Al^{(IV)}$ and $Al^{(VI)}$-$Al^{(IV)}$ diagrams (Fig. 9c, d) amphiboles follow the pargasitic substitution, with Amp_{Sym} that shows the highest $Al^{(IV)}$ and $Al^{(VI)}$ concentrations.

In chlorite peridotites olivine, orthopyroxene and Opx_{Porph} all show X_{Mg} ranging between 0.90 and 0.91, and clinopyroxene is diopside-rich ($Di_{90}Jd_4Hd_6$, Tab. 3). In the Si-Al diagram the two orthopyroxene generations of chlorite peridotite overlap the composition of orthopyroxenes of garnet peridotite B3A (light grey symbols in Fig. 9b). Porphyroblastic amphibole in equilibrium with Opx_{Porph} and Phl_{Porph} is a hornblende (Amp_{Porph}, Tab. 3), whereas Amp_2 in the recrystallised matrix and Amp_3 along the chlorite foliation vary in composition from edenite to tremolitic-hornblende. In the Na-$Al^{(IV)}$ and $Al^{(VI)}$-$Al^{(IV)}$ diagrams (Fig. 9c, d) also amphiboles of the chlorite peridotite plot along the pargasite exchange vector.

6.1.2. Tremolitite

Relict amphibole porphyroblasts in tremolitites are hornblende and their compositional variation is closely related to the optical zoning (Tab. 3). The analysed dusty cores correspond to Mg-hornblende while the inclusion-free rims are tremolites (Fig. 9c) with compositions resembling those of retrogression tremolites, characterised by lower Al, Na and Fe content with respect to porphyroblastic hornblende (Tab. 3, Fig. 9c, d).

7.1.3. Eclogites

In both mafic and kyanite-bearing eclogites, garnets are zoned and their core-to-rim composition varies from $Py_{35}Alm_{40}Gr_{25}$ to $Py_{28}Alm_{52}Gr_{20}$ at rim (Tab. 3). The composition of omphacite included in garnet corresponds to $Di_{60}Jd_{30}Hd_{10}$, whereas Cpx_2 in symplectites is diopside-rich ($Di_{80}Jd_6Hd_{14}$; Tab. 3). In the Na versus $Al^{(VI)}$ variation diagram (Fig. 10a) clinopyroxenes show a decrease of Na and $Al^{(VI)}$ from omphacites to symplectitic diopsides.

All amphiboles in eclogites are calcic. Amphiboles after garnet and omphacite (Amp_2) vary from Mg-hornblende to actinolite, whereas coronitic Amp_3 varies in composition from pargasite to Mg-hornblende to tremolite (Tab. 3). In the Na-$Al^{(IV)}$ and $Al^{(VI)}$-$Al^{(IV)}$ variation diagrams of Figures 10b and c, both Amp_2 and Amp_3 plot along the pargasite exchange vector. Amp_3 shows a variable Na-$Al^{(IV)}$ trend depending on its microstructural site. Coronitic amphiboles around symplectites post-omphacite in fact show the highest Na concentration, comparable to some grains included in garnet representing retrogressed omphacites. In mafic eclogite, porphyroblastic K-feldspar corresponds to almost pure orthoclase X_{Or} = 0.98. Slightly lower X_{Or} = 0.90 characterises Kfs_M occurring within the melt pockets and patchy zone aggregates together with Cpx_M + Q_M + Pl_M in high-Al_2O_3 eclogites (c.f. Tab. 3 and Tumiati et al., 2018).

6.2. Trace elements

The trace elements compositions of analysed rock forming minerals are listed in Table 4 and portrayed in Figure 11 and 12.

6.2.1. Peridotites

Garnet from garnet peridotites shows the classic REE pattern with enrichment in HREE (up to 10×PM) and depletion in LREE (dark grey area in Fig. 11a). Clinopyroxenes (white area in Fig. 11a) and pargasites (Amp_1) of sample B3A (green circles and diamonds in Fig.11a) display REE patterns characterised by relative depletions in HREE ($La_N/Er_N \approx 3$), indicating that they grew in chemical equilibrium with garnet. They also show high LREE and MREE concentrations reflecting the enrichment in LREE of the bulk rock (c.f. Fig. 8a). In sample A2C2 Amp_1 is zoned with REE patterns (yellow circles and diamond in Fig. 11a) enriched in HREE with respect to Amp_1 of sample B3A. This different HREE fractionation is in contrast with the microstructural observation that this Amp_1 is in equilibrium with garnet (Fig. 5a) and likely indicates that an equilibration with post-peak minerals already occurred. As shown in Tab. 4, orthopyroxene is generally depleted in all incompatible elements. In terms of other trace elements, both garnet and clinopyroxene display a general depletion in LILE whereas amphibole of B3A is slightly enriched in LILE with K and Pb ≈ 10×PM (Fig. 11b). Also concerning the LILE, amphibole of sample A2C2 displays a different pattern with higher LILE concentrations (up to 200×PM) with respect to amphibole of sample B3A.

In chlorite peridotites (DB113), porphyroblastic amphibole (Amp_{Porph}) in equilibrium with Opx_{Porph} and Phl_{Porph} (Fig. 5c) has been analysed and its REE pattern is enriched in LREE with respect to HREE (Fig. 11c; Tab. 4). Its LILE concentrations reaches only up to 10×PM with a strong Ba negative anomaly. Opx_{Porph} growing at the expenses of olivine shows LREE contents just above the detection limit, with $La_N/Ce_N = 1.9$ (Fig. 11c, Tab. 4). Chl_3 from the retrogressed chlorite foliation represents the major host of fluid mobile elements displaying high Cs, Rb and K (Cs up to 300×PM), a negative anomaly in Ba and positive U/Th ratios (Fig. 11d).

In tremolitites, the REE patterns of Mg-hornblende porphyroblasts and tremolite neoblasts closely match that of the bulk-rock (c.f. Fig. 8c) showing higher LREE (maximum La = 5×PM) with respect to the HREE (Fig. 11e). Concerning the LILE, both amphibole generations show concentrations up to 10×PM with a strong Ba negative anomaly and a relatively high U/Th ratio (Fig. 11f).

6.2.2. Eclogites

Garnets from all eclogite samples have HREE-enriched and LREE-depleted patterns with REE normalised concentrations up to 20×PM. Garnets from mafic eclogites display variable HREE concentrations with Lu varying from 4 to 14×PM but no important differences are observed between analysed cores and rims (Fig. 12a). By contrast, garnets of kyanite-bearing eclogites show a relative enrichment in MREE and a sharp core-to-rim zonation with progressive depletion in HREE (cores: Lu = 8×PM; rims: Lu =2-4×PM; Fig. 12b). In terms of other trace elements garnet is depleted in LILE except for Cs and Pb (Tab. 4). Zoisite from mafic eclogite D6 is almost homogeneous in composition and a slight difference in Yb concentration can be observed between core and rim (Fig. 12c). Zoisite has REE absolute concentrations up to 11000×PM with a slight fractionation between LREE and HREE (e.g. La_N/Yb_N = 5.3×PM). Allanite growing around zoisite (Fig. 6b) shows REE concentrations up to 40000×PM, with strong enrichement in LREE (Fig. 12d). Amp_2 of the lower pressure paragenesis was too small to be analysed. We therefore portray in Figure 12e and 12f only the patterns of coronitic Amp_3. All amphiboles display a relative enrichment in MREE with respect to HREE, resembling that of garnet from kyanite-eclogite (Fig. 12e). Amp_3 represents the major host of fluid mobile elements with spikes in Rb and K and high U/Th ratio and is likely the responsible for the LILE enrichment of the bulk rock (Fig. 12f).

7. Discussion

Numerous field-based, petrological and geochemical studies have described the chemical interaction between mantle peridotites and felsic continental crust via aqueous fluids, melts and supercritical liquids released at HP and UHP conditions, during prograde or retrograde metamorphism along a subduction pathway (e.g. Rampone and Morten, 2001; van Roermund et al., 2002; Scambelluri et al., 2006; Janák et al., 2006; Malaspina et al., 2006, 2017; Tumiati et al., 2007; Scambelluri et al., 2008; Malaspina et al., 2010; Gudelius et al., 2019). Concerning the Alpine belt, the best examples of suprasubduction garnet peridotites metasomatised by crust-derived agents at HP are represented by occurrences in the Eastern and Central Alps at Pohorje (Janák et al., 2006), Ulten Zone (Rampone and Morten, 2001; Scambelluri et al., 2006; Tumiati et al., 2007; Gudelius et al., 2019), Alpe Arami (Nimis and Trommsdorff, 2001; Paquin and Altherr, 2001) and Monte Duria (Fumasoli, 1974; Evans and Trommsdorff, 1978; Hermann et al., 2006). They all show evidence for metasomatism by the presence of metasomatic phases like amphibole, phlogopite, dolomite and REE-minerals (Tumiati et al., 2005; Lavina et al., 2006; Sapienza et al., 2009; Malaspina and Tumiati, 2012) and by the whole rock enrichment of some incompatible elements such as LREE (Rampone and Morten, 2001; Scambelluri et al., 2006; Tumiati et al., 2007; Gudelius et al., 2019). Similarly to Ulten zone amphibole+garnet peridotites, Monte Duria garnet peridotites and the retrogressed chlorite peridotites show abundant porphyroblasts of pargasitic amphibole, dolomite, phlogopite and porphyroblastic orthopyroxene forming at the expenses of a previous olivine (Fig. 5a-d), indicating that they experienced metasomatism and interaction with crust-derived agents, enriched in SiO_2, Al_2O_3, K_2O, CO_2 and H_2O. Similar features in metasomatised suprasubduction peridotites have been described by Malaspina et al. (2006) and Endo et al. (2015) who demonstrated that replacive orthopyroxene derives by the reaction of the peridotite with a slab-derived silicate melt at HP/UHP. In addition, experimental results on olivine solubility in COH fluids (Tiraboschi et al., 2018) and mass balance modelling of solid-solution equilibrium between slab-derived aqueous fluids and garnet peridotite (Campione et al., 2017) indicate that also H_2O-rich fluids released from a subducted eclogite are able to crystallise metasomatic orthopyroxene in the mantle. Whether the metasomatic agent responsible for the modal metasomatism of Monte Duria peridotites is a C-bearing silicate melt or an aqueous COH fluid (Hermann et al., 2006) must be searched in the associated crustal rocks and in their reconstructed P-T path.

Further evidence of metasomatism recorded by Monte Duria garnet peridotites is the peculiar fractionation of LREE (La_N/Nd_N = 2.4; Fig. 8a) related to the LREE enrichment in Cpx_1 and Amp_1, both crystallised in the garnet stability field, as shown by the relative depletion in HREE (Fig. 11a). The "spoon-shaped" LREE pattern of Monte Duria peridotites strongly resembles that of the Ulten Zone peridotites (pink area in Fig. 8a), which has been interpreted as acquired by the interaction with a hydrous melt (Rampone and Morten, 2001; Scambelluri et al., 2006). Interestingly, Monte Duria peridotites also show a selective enrichment in some LILE (Fig. 8b), which were mainly incorporated by those amphiboles equilibrated in the spinel stability field. Indeed, as shown in Figure 11a and b, the most LILE enriched Amp_1 (yellow symbols) shows HREE enriched patterns indicating non-equilibrium with garnet. This observation suggests that the LREE and LILE enrichment occurred at different pressure conditions (garnet and spinel stability fields) and likely by different metasomatic agents, silicate melt and aqueous fluids, respectively.

7.1 The HP partial melting of Borgo eclogites

In the Monte Duria area, garnet peridotites occur embedded in low-grade migmatitic gneiss (Mt. Duria) or in direct contact with variably migmatised HP mafic rocks (Borgo). Bulk rock and mineral phase assemblages indicate that these mafic migmatites derive from an eclogite precursor, with a basaltic or gabbroic protolith (Tab. 2 and Fig. 7 and 8e). Peridotites and HP mafic migmatites of Borgo share a common metamorphic evolution, reaching peak conditions at 2.5-3 GPa and 750-800 °C and post-peak static equilibration at 0.8-1 GPa and 850 °C (Tumiati et al., 2018). Field occurrence of mafic rocks in Borgo indicates that partial melting started in a deformation regime that is neither related to the shear zone at the contact with migmatitic gneiss (Fig. 2 and Fig. S-1a), nor to the static re-equilibration at HT conditions, recorded by sapphirine-baddeleyite-srilankite and sapphirine-corundum assemblages in coronas around garnet (peridotites) and kyanite (eclogites), respectively (Tumiati et al., 2018). Moreover, the strong layered structure of melanosome and leucosome containing zoisite, omphacite and garnet of amphibole-bearing migmatites (Fig. 4d), along with the occurrence of peculiar deformation structures like lobes and cusps, characteristics of syn-melting deformation (Fig. 4e; McLellan, 1989), strongly suggest that Borgo eclogitic rocks underwent partial melting during prograde-to-peak HP metamorphic conditions. Field structures are supported by microstructural evidence in eclogite boudins enclosed in amphibole-bearing migmatites. Both mafic (D6) and high-Al_2O_3 (D9) eclogites show thin films of clinopyroxene + K-feldspar around both quartz relicts and symplectite aggregates post-omphacite (Fig. 6a,c), together with interstitial pocket aggregates of K-feldspar + plagioclase + quartz + clinopyroxene (Fig. 6d). The reported mineral assemblages closely resemble the ones reported in multiphase melt inclusions trapped by zircons from eclogites of Eastern Papua new Guinea, which underwent partial melting during the beginning of hexumation (DesOrmeau, 2018). Also the microstructural features constraining the direct observation of HP partial melting of eclogites are in agreement with the ones reported in the Central Sulu Orogen by Wang et al. (2014), who recognised melt droplets of leucosome composed of quartz-plagioclase-K-feldspar formed along grain boundaries in the eclogites of the General's Hill. Interestingly, our Cpx_M + Kfs_M rims (Fig. 6c) and Kfs_M + Pl_M + Qz_M + Cpx_M pockets (Fig. 6d) are preferentially oriented parallel to the HP foliation of the high-Al_2O_3 eclogites, suggesting that the crystallisation of these microstructures was sin-kynematic to the HP deformation regime that led to the formation of the Ky + Omp + Qz + Zo ± Kfs assemblage. Moreover, similar evidence of viscous shearing syn-kinematic melt-rock interaction during the infiltration of a felsic melt in mafic rocks has been reported in the Seiland Igneous Province, northern Norway (Degli Alessandrini et al., 2017). In this work a polyphase mixture of clinopyroxene + orthopyroxene + plagioclase + quartz + ilmenite ± K-feldspar wrap porphyroclasts of orthopyroxene, clinopyroxene and plagioclase along the mylonitic foliation and pools of former melt are preserved as K-feldspar surrounding rounded plagioclase and quartz grains.

The partial melting of MORB systems at HP has been experimentally studied by several works (e.g. Lambert and Wyllie, 1972; Schmidt and Poli 1998; Yaxley and Green, 1998; Rapp et al., 1999; Schmidt et al., 2004; Kessel et al., 2005; Klimm et al., (2008); Liu et al., 2009), giving indication on the P-T conditions at which eclogites undergo flush or fluid absent melting in subduction zones. As pointed out by Schmidt and Poli (2014), fluid-saturated melting of K-bearing basaltic rocks can be achieved at 650 °C and 1.5 GPa, reaching 750 °C at 3 GPa and ending at 950 °C and 5.5 GPa by the addition of an aqueous fluid from the external system (Lambert and Wyllie, 1972; Schmidt and Poli, 1998; Schmidt et al., 2004). At higher pressures, fluid absent melting of K-bearing MORB is mainly controlled by the dehydration of phengite, which starts at 850 °C and 2-2.5 GPa and continues up to 900-950 °C at 3 GPa (Hermann and Green, 2001; Liu et al., 2009). In Figure 13 we portrayed the peak conditions recorded by our samples (green is Mt. Duria garnet peridotite, red is Borgo eclogite) compared with the P-T conditions of wet and dry basalt solidi, along with the phengite dehydration melting for a MORB composition. The stable paragenesis at the peak conditions (750 °C and 3 GPa; Tumiati et al., 2018) is represented by garnet + omphacite + kyanite + zoisite + K-feldspar + quartz/coesite (Tab. 1 and Fig. 6; Fig. 6d of Tumiati et al., 2018). The presence of K-feldspar relict porphyroblasts instead of phengite suggests that the eclogites were almost dry at peak conditions. Indeed, the K-feldspar composition of Borgo eclogites (X_{Or} = 0.98) indicates its stability with a garnet + omphacite + kyanite + quartz at average H_2O content of 0.05 wt.% at P = 3 GPa and T = 750 °C (Tumiati et al., 2018). These observations, therefore, preclude the possibility that our eclogites underwent phengite dehydration melting, because the temperature equilibration conditions recorded by the peak mineral assemblage are too low.

As shown in Figure 13, the P-T peak conditions of Borgo eclogites are slightly beyond the wet basalt solidus, thus suggesting that the partial melting occurred at fluid present conditions. It must be considered that Monte Duria area garnet peridotites record a first hydration stage in a static regime given by chlorite pseudomorphic crystallisation on garnet (Chl_1) predating the development of a penetrative LP-LT chlorite foliation (Chl_3) cutting the garnet layering (Fig. 3c, d, S-2a, d). Moreover, some garnets of Mt. Duria peridotites show Chl_1 pseudomorphs partly overgrown by orthopyroxene + spinel symplectites, in turn surrounded by spinel-amphibole kelyphitic corona (Fig. S-2a, b, c), suggesting that a hydration event occurred before the LP-(U)HT metamorphic event at 850 °C and 0.8-1 GPa (Tumiati et al., 2018). Because at the peak conditions of both peridotites and eclogites chlorite is stable in an ultramafic system (Fumagalli and Poli, 2005; grey curve of Fig. 13), the hydration event likely occurred at HP led to the chloritisation of garnets in the peridotites and flushed the associated eclogites, therefore triggering partial melting.

Melting of mafic crust at high pressures produces the so-called adakites, which are characterised by a peculiar geochemical imprint, with high SiO_2, Al_2O_3, La/Yb and Sr/Y, coupled with low Y and Yb concentrations (Drummond et al. 1996; Schmidt and Poli, 2014). The comparison between the major element compositions of the melt pockets in eclogite of Borgo (D9 in Tab. 2; Fig. 6c,d and S-3) and the composition of archean adakite and low-Al trondhjemite-tonalite-dacite (TTD) of Drummond et al. (1996) show some similarities between the two sample groups. In terms of major element composition, a significant difference is the CaO content, which is higher in our melt pockets, likely due to the occurrence of several clinopyroxene grains, and the Na_2O/K_2O ratio, which is >>1 for archean adakite and ≈ 0.5 for our leucosome. This difference is due to the fact that omphacite is still stable (in the presence of K-feldspar) in the residual eclogite (Tumiati et al., 2018) that retains Na_2O from the melt, with $Na^{cpx/melt}$ partition coefficient close to unity at 3 GPa (Schmidt et al. 2004), supporting that the partial melting of Borgo mafic rocks occurred at high pressure. In terms of trace elements, instead, Borgo leucosome shows very different La/Yb = 0.1, Sr/Y = 8.16, Zr/Sm (8.2) vs La/Sm (0.24) ratios with respect to adakites *l.s.* of Drummond et al. (1996). These differences are mainly due to the strong partitioning of LREE and Sr into the residual allanite and zoisite, respectively, in the resitic portions of eclogites as shown in Figure 8e, f. This partitioning results in a relative enrichment of HREE of our lecusome despite the occurrence of garnet (together with zoisite and allanite) in the residue.

7.2 Melt/rock interaction and formation of garnet websterites

The contact between the chlorite peridotite body of Borgo and the HP mafic migmatites is marked by the occurrence of a tremolitite layer (Fig. 2, S-1b). Such rocks also occur as variably stretched layers within the peridotite body (Fig. 4a-c) showing sharp contacts with the host peridotite and a marked boudinage parallel to the garnet layering of the peridotite. The now retrogressed garnet-bearing foliation of the peridotite, in fact, wraps the boudins and is deflected into the necks (Fig. 4b, c), indicating that the tremolitite boudinage occurred during a deformation event when Borgo peridotites were in the garnet stability field. These layers display relict Mg-hornblende extensively overgrown by tremolite and contain Phl_3 + Chl_3 + Tc + Tr pseudomorphs after garnet (Fig. 5e, f). As shown in Fig. 5e, the crystallisation of tremolite and chlorite occurred in a static regime together with the pseudomorphic replacement of garnets. This indicates that the Phl_3 + Chl_3 + Tc + Tr mineral assemblage of the tremolitite layers postdates the boudinage deformation event, suggesting that they derive from a precursor that during the formation of the peridotite garnet-foliation was more rigid than the host peridotite. Two hypotheses may explain these structural and microstructural observations. The first one is that the tremolitites of Borgo derive from a Mg-hornblende-bearing precursor as indicated by the presence of relict Mg-hornblende porphyroblasts (Fig. 5e). The alternative hypothesis is that the tremolitites derive from a garnet websterite with a relatively high clinopyroxene modal content. In both cases, these hybrid layers, characterised by high Mg# (>90, Fig. 7a) and high CaO (12.38 wt%, Fig. 7b) formed in the garnet stability field, and subsequently retrogressed in tremolitites during the LP-LT re-equilibration at fluid-present conditions.

The peculiar hybrid composition of the tremolitite layers strongly suggests that they formed after the reaction between the eclogite leucosome and the garnet peridotite at HP (Fig. 7). To test this hypothesis, we modelled the mineral assemblage that would be thermodynamically stable when the pristine garnet peridotite (composition of A2C2, Tab. 2) chemically mixes with a felsic adakite-like melt (HP melt pockets in D9 eclogite, Tab. 2). The result is shown in Figure 14a, where the weight fraction (X) of different degrees of chemical mixing between the garnet peridotite (X = 0) and the eclogite leucosome (X = 1) is plotted versus the activity of water (log aH$_2$O) at fixed P-T conditions corresponding to the peak recorded by both peridotite and eclogite. We also assume that most of infiltrating melt is consumed in the reactions. This assumption is supported by field observations that show no evidence of preserved eclogite-derived melt within the peridotite bodies.

At X = 0 (no melt infiltration), and aH$_2$O = 0.02 the garnet peridotite is represented by the olivine + orthopyroxene + clinopyroxene + garnet + phlogopite mineral assemblage. At higher water activities (aH$_2$O > 0.4) pargasitic amphibole is stable, while at the maximum water activity (aH$_2$O > 0.9) chlorite is stable together with pargasite and phlogopite. This scenario is supported by the petrographic and microstructural evidence that Chl$_1$ forms at HP and at water saturated conditions after the prograde-to-peak Amp$_1$ formation (Tab. 1, Fig. 5a, b, Fig. S-2a). Additional clino- and orthopyroxene are expected to form when the peridotite composition is mixed with increasing weight fraction of leucosome, reaching the maximum modal proportion at X = 0.45 (31 Cpx vol% and 40 Opx vol%). In addition, for X = 0.45 and aH$_2$O > 0.4 chlorite and olivine are not stable. The presence of high modal amounts of porphyroblastic orthopyroxene, amphibole and phlogopite growing at the expenses of relict olivine and orthopyroxene in Borgo peridotite (Fig. 5c) close to the contact with inner tremolitite layers (location of DB113 in Fig. 2) indicates mixing of more than 35 wt% of leucosome with the garnet peridotite (Fig. 14a). Therefore, from a structural and thermodynamic point of view, the tremolitite layers likely derive from a previous garnet websterite or garnet amphibole-phlogopite-bearing websterite, depending on the water activity of the melt infiltrating the garnet peridotite. It is worth noting that the trace element composition of relict hornblende of the tremolitite DB148 and the metasomatic porphyroblastic amphibole of DB113 peridotite are identical, both in terms of REE (Fig. 11c, e) and LILE (Fig. d, f).

A metasomatic origin for clinopyroxenites/websterites with a similar major element compositions has been also proposed for group D-Ronda pyroxenites of the Betic Cordillera, Southern Spain (Garrido and Bodinier, 1999), for the supra-subduction San Jorge and Santa Isabel pyroxenites of Solomon Islands, West Pacific (Berly et al., 2006) and for peridotite-hosted garnet clinopyroxenites from the Granulitgebirge in the Bohemian Massif, central Europe (Borghini et al., 2018). These pyroxenites are characterised by high Mg#, CaO > 10 wt% and $Al_2O_3 \approx 2$ wt% similarly to our tremolitite (Tab. 2, Fig. 5).

It is worth noting that Borgo peridotite shows several dolomite crystals in equilibrium with amphibole and chlorite (Fig. 5d), indicating that the melt interacting with the peridotite carried additional CaO and CO_2. The water-assisted retrogression of the hybrid garnet ±amphibole-bearing websterite has been modelled in Figure 14b, where the T-X section of the peridotite-leucosome mixing in the representative range of $0<X<0.5$ has been calculated at H_2O saturated condition at P = 0.7 GPa, interpreted as the beginning of retrogression after the HT event (Fig. 13). Even considering the uncertainties of some solid solution models (e.g. amphibole, see Tumiati et al., 2013), this pseudosection indicates that tremolitic amphibole (80 to 90 mol.% of tremolite) forms when metasomatic websterites equilibrate at LP-LT conditions.

As summarised in Table 1 and supported by structural, microstructural, chemical and thermodynamic evidences, a HP hydration event formed static chlorite on garnets of the Monte Duria peridotites (Fig. 3c, S-2) and flushed the associated eclogites. At 3 GPa and 750 °C water saturated eclogites underwent partial melting (Fig. 4d, e), producing Ca-rich leucosomes (Fig. 6a, c, d), which reacted with the associated garnet peridotite forming garnet-amphibole-phlogopite websterites (Fig. 4a-c and 5c) and dolomite in the chlorite peridotite (Fig. 5d). The melt-rock interaction occurred at high deformation regimes, yielding to the formation of garnet layering in the peridotite and the consequent boudinage of the websterite, particularly in the layers within the garnet peridotite (Fig. 2 and 4b). The garnet peridotite and associated (partially melted) eclogites subsequently underwent decompression in the spinel stability field (Fig. 5b) forming symplectites after garnet and omphacite (Fig. 6e, f; Tumiati et al., 2018). Water-absent LP-HT re-equilibration at 1 GPa and 850 °C crystallised sapphirine-baddeleyite-srilankite coronas around garnet in the peridotites and sapphirine-corundum coronas around kyanite in eclogites (Tumiati et al., 2018). Finally, a LP-LT water-present deformation event formed a chlorite foliation cutting the garnet layering in the peridotites (Fig. 3c, d), yielded to the hydration of the amphibole-phlogopite bearing websterites with the crystallisation of tremolite and Phl_3 + Chl + Tc + Tr pseudomorphs after garnet (Fig. 5e, f) and the formation of amphibole (Amp_3) coronas around symplectites after omphacite in the eclogites.

8. Deformation-induced melt/peridotite reaction at the slab-mantle interface

The fate of slab-derived melts in the overlying mantle and their capability to transport crustal components to the mantle wedge is still poorly known. As shown by Spandler and Pirard (2013), crustal melts may migrate into the mantle by porous flow, focussed flow and diapiric flow, depending on their composition, and therefore reactivity, with ultramafic rocks and also by porosity of the mantle. Porous flow produces a strong metasomatism, forming almost monomineralic orthopyroxene and phlogopite layers at the slab-mantle interface, limiting the mass transport of crustal elements except those filtered into residual aqueous fluids (Malaspina et al., 2006; 2009). Focussed flow is represented by the direct transfer of slab melt from the top of the slab to the mantle wedge, forming a network of pyroxenite veins, limiting the melt-peridotite reaction only to minor interaction products (pyroxenes and amphiboles) at the wall rock (e.g. Arai et al., 2003; Kepezhinskas et al., 1995). Finally, diapiric flow may occur after the detachment of sediments + serpentinite rich mélange due to buoyancy of diapirs which undergo partial melting in the mantle wedge (e.g., Marschall and Schumacher, 2012; Tumiati et al., 2013). It must be specified that all these models consider melting of sediment-like systems of the subducting slab.

The direct evidence of eclogite melting during subduction has been reported by Wang et al. (2014) and the interaction of the mantle with mafic melts at high pressure was experimentally studied by Wang et al. (2016) at 1 GPa and 1200 °C and Perchuk et al. (2018) at 2.9 GPa and 750-900 °C. In these studies the reaction with mafic melts produces harzburgite and then orthopyroxenite layers. Interestingly, experiments performed at P-T conditions closed to the peak recorded by eclogites and garnet peridotites of Monte Duria (3 GPa and 750 °C) show reaction zones at the metabasite-peridotite interface with formation of orthopyroxene ± magnesite ± garnet and layers of newly-formed omphacite ± garnet ± phlogopite + orthopyroxene + magnesite by focused flow (Perchuk et al., 2018). Similar mineral associations occur at the contact between Borgo peridotite and inner tremolitite layers (Fig. 5c, d) and in the modelled mineral assemblage of tremolitites before the later hydration (Fig. 14).

The interaction between mafic melts and peridotite in a deformation regime (i.e. during the formation of extensional shear zones) has been widely studied in natural case studies, and experimentally and theoretically modelled, in lithospheric and sub-oceanic mantle (e.g. Garrido and Bodinier, 1999; Liang et al., 2010; Gysi et al., 2011; Baltzell et al. 2015). Regardless of the composition of the melts, experiments and numerical modelling evidenced the role of shear rates in the “compaction-decompaction” porosity bands in the peridotite, favouring melt migration and solubility gradients at increasing deformation (Liang et al., 2010; Baltzell et al. 2015). Following a similar mechanism, the development of alternating pyroxenite (l.s.) bands in the peridotite of Borgo (Fig. 2 and 4a-c) may have been favoured by melt-peridotite interaction during shearing. This interpretation is reported in Figure 15, which portrays a conceptual model of the interaction of eclogite-derived melt and overlying peridotite during the shearing induced by slab subduction and/or mantle corner flow. Evidence of syn-deformation melt-rock interaction is given by the occurrence of boudinage of our metasomatic layers, parallel to and wrapped by the garnet foliation of the host peridotite, indicating a shearing induced weakening of the garnet peridotite. Such mechanism has been reported by a recent work of Tommasi et al. (2017), who demonstrated that the occurrence of hydrous melts during shearing strongly changes the deformation processes in mantle peridotites. Following these authors (Tommasi et al., 2017), accomodation of deformation by peridotite results from stress-controlled dissolution and precipitation and advective transport of chemical components by the melts. Moreover, the presence of hydrous melts also favours fast grain boundary migration producing strong rheological weakening of the garnet peridotite. The focussed flow of slab melts into the mantle, instead of porous flow, may therefore occur when the overlying mantle peridotite undergoes shearing and weakening. In conclusion, the application of well studied syn-kynematic melt-rock reaction models in sub-continental and oceanic mantle environment to subduction environments may represent a further step to unravel the mechanism of initiation of mass transport from subducted eclogites to the supra-subduction mantle wedge occurring at the slab-mantle interface.

Acknowledgments

We thank A. Risplendente for the assistance with the scanning electron microscope and electron microprobe, and S. Poli and A. Zanchi for funding support and constructive discussion. We acknowledge J. Hermann and E. Rampone for very critic and constructive reviews that helped to much improving the paper. This work was funded by Italian Ministry of University and Research (PRIN 2017 - Prot. 2017ZE49E7_005) and also benefited from the Deep Carbon Observatory (DCO) and University of Milano-Bicocca 2016-ATE-0222 and 2018-ATE-0087.

References

Arai, S., Shimizu, Y., Gervilla, F., 2003. Quartz diorite veins in a peridotite xenolith from Tallante, Spain: implications for reaction and survival of slab-derived SiO2- oversaturated melt in the upper mantle. Proceedings of the Japan Academy, Series B, 79, 146–150.

Arcay, D., Tric, E., Doin, M.P., 2007. Slab surface temperature in subduction zones: Influence of the interplate decoupling depth and upper plate thinning processes. Earth Planet. Sci. Lett. 255, 324–338

Baltzell, C., Parementier, E.M., Liang, Y., Tirupathi, S., 2015. Geochemistry, Geophysics, Geosystems. Geochem. Geophys. Geosyst. 18, 1541–1576.

Biino, G.G., Marquer, D., Nussbaum, C., 1997. Alpine and pre-Alpine subduction events in polycyclic basements of the Swiss Alps. Geology 25, 751.

Borghini, A., Ferrero, S., Wunder, B., Laurent, O., Brien, P.J.O., Ziemann, M.A., 2018. Granitoid melt inclusions in orogenic peridotite and the origin of garnet clinopyroxenite. Geology 46, 1–4.

Brenker, F.E., Brey, G.P., 1997. Reconstruction of the exhumation path of the Alpe Arami garnet-peridotite body from depths exceeding 160 km. J. Metamorph. Geol., 15(5), 581-592.

Brueckner, H.K., Medaris, G., 2000. A general model for the intrusion and evolution of 'mantle' garnet peridotites in high-pressure and ultra-high-pressure metamorphic terranes. J. Metamorph. Geol. 18, 123–133.

Burri, T., Berger, A., Engi, M., 2005. Tertiary migmatites in the Central Alps: regional distribution, field relations, conditions of formation, and tectonic implication. Schweiz. Mineral. Petrogr. Mitt. 85, 215–232.

Campione M, Tumiati S, Malaspina N, 2017. Primary spinel + chlorite inclusions in mantle garnet formed at ultrahigh-pressure. Geochemical Perspective Letters 4, 19–23.

Dale, J., Holland, T.J.B., 2003. Geothermobarometry, P-T paths and metamorphic field gradients of high-pressure rocks from the Adula nappe, Central Alps. J. Metamorph. Geol. 21, 813–829.

Degli Alessandrini G, Menegon L, Malaspina N, Dijkstra A, Anderson M, 2017. Creep of mafic dykes infiltrated by melt in the lower continental crust (Seiland Igneous Province, Norway). Lithos 274–275, 169–187.

Del Moro, A., Martin, S., & Prosser, G. (1999). Migmatites of the Ulten Zone (NE Italy), a record of melt transfer in deep crust. J. Petrol., 40(12), 1803-1826.

DesOrmeau, J.W., Gordon, S.M. Little, T.A., Bowring, S.A., Schoene, B., Samperton, K.M., Kylander-Clark, A.R.C. (2018) Using Eclogite Retrogression to Track the Rapid Exhumation of the Pliocene Papua New Guinea UHP Terrane. J. Petrol., 59, 2017-2042.

Drummond, M.S., Defant, M.J., Kepezhinskas, P.K., 1996. Petrogenesis of slab-derived trondhjemite-tonalite-dacite / adakite magmas. Trans. R. Soc. Edinb. Earth Sci. 87, 205–215.

Endo, S., Mizukami, T., Wallis, S.R., Tamura, A., Arai, S., 2015. Orthopyroxene-rich Rocks from the Sanbagawa Belt (SW Japan): Fluid–Rock Interaction in the Forearc Slab–Mantle Wedge Interface. J. Petrol. 56, 1113–1137.

Ernst, W. G. (1978). Petrochemical study of lherzolitic rocks from the Western Alps. J. Petrol., 19(3), 341-392.

Evans, B.W., Trommsdorff, V., 1978. Petrogenesis of garnet lherzolite, Cima di Gagnone, Lepontine Alps. Earth Planet. Sci. Lett. 40, 333–348.

Fumagalli, P., Poli, S., 2005. Experimentally Determined Phase Relations in Hydrous Peridotites to 6.5 GPa and their Consequences on the Dynamics of Subduction Zones. J. Petrol. 46, 555–578.

Fumasoli, M.W., 1974. Geologie des Gebietes nördlich und südlich der Jorio-Tonale-Linie im Westen von Gravedone (Como, Italia). Dissertation, Universität Zürich.

Gale, A., Dalton, C. A., Langmuir, C. H., Su, Y., & Schilling, J. G. (2013). The mean composition of ocean ridge basalts. Geochem. Geophys. Geosyst. 14(3), 489–518.

Galli, A., Le Bayon, B., Schmidt, M.W., Burg, J.P., Caddick, M.J., Reusser, E., 2011. Granulites and charnockites of the Gruf Complex: Evidence for Permian ultra-high temperature metamorphism in the Central Alps. Lithos 124, 17–45.

Galster, F., Cavargna-Sani, M., Epard, J., Masson, H., 2012. New stratigraphic data from the Lower Penninic between the Adula nappe and the Gotthard massif and consequences for the tectonics and the paleogeography of the Central Alps. Tectonophysics 579, 37–55.

Gillis, K.M., Snow, J.E., Klaus, A., Abe, N., Adrião, Á.B., Akizawa, N., Ceuleneer, G., Cheadle, M.J., Faak, K., Falloon, T.J., Friedman, S.A., Godard, M., Guerin, G., Harigane, Y., Horst, A.J., Hoshide, T., Ildefonse, B., Jean, M.M., John, B.E., Koepke, J., MacHi, S., Maeda, J., Marks, N.E., McCaig, A.M., Meyer, R., Morris, A., Nozaka, T., Python, M., Saha, A., Wintsch, R.P., 2014. Primitive layered gabbros from fast-spreading lower oceanic crust. Nature 505, 204–207.

Gudelius, D., Aulbach, S., Braga, R., Ho, H.E., Woodland, A.B., Gerdes, A., 2019. Element Transfer and Redox Conditions in Continental Subduction Zones : New Insights from Peridotites of the Ulten Zone , North Italy. J. Petrol. 60, 231–268.

Heinrich, C.A., 1986. Eclogite facies regional metamorphism of hydrous mafic rocks in the Central Alpine Adula nappe. J. Petrol. 27, 123–154.

Hermann, J., Rubatto, D., Trommsdorff, V., 2006. Sub-solidus Oligocene zircon formation in garnet peridotite during fast decompression and fluid infiltration (Duria, Central Alps). Mineral. Petrol. 88, 181–206.

Herwartz, D., Nagel, T.J., Münker, C., Scherer, E.E., Froitzheim, N., 2011. Tracing two orogenic cycles in one eclogite sample by Lu–Hf garnet chronometry. Nat. Geosci. 4, 178–183.

Kessel, R., Schmidt, M.W., Ulmer, P., Pettke, T., 2005. Trace element signature of subduction-zone fluids, melts and supercritical liquids at 120-180 km depth. Nature 437, 724–7.

Klimm, K., Blundy, J. D., & Green, T. H. (2008). Trace element partitioning and accessory phase saturation during H2O-saturated melting of basalt with implications for subduction zone chemical fluxes. J. Petrol. 49(3), 523–553.

Lavina, B., Carbonin, S., Russo, U., Tumiati, S., 2006. The crystal structure of dissakisite-(La) and structural variations after annealing of radiation damage. Am. Mineral. 91, 104–110.

Liati, A., Gebauer, D., 2003. Geochronological constraints for the time of metamorphism in the Gruf Complex (Central Alps) and implications for the Adula-Cima Lunga nappe system. Schweiz. Mineral. Petrogr. Mitt. 83, 159–172.

Liati, A., Gebauer, D., Fanning, C.M., 2009. Geochronological evolution of HP metamorphic rocks of the Adula nappe, Central Alps, in pre-Alpine and Alpine subduction cycles. J. Geol. Soc. London. 166, 797–810.

Liu, Q., Jin, Z., Zhang, J., 2009. An experimental study of dehydration melting of phengite-bearing eclogite at 1.5-3.0 GPa. Chinese Sci. Bull. 54, 2090–2100.

Malaspina, N., Hermann, J., Scambelluri, M., 2009. Fluid/mineral interaction in UHP garnet peridotite. Lithos 146-147, 11-17.

Malaspina, N., Hermann, J., Scambelluri, M., Compagnoni, R., 2006. Polyphase inclusions in Garnet-Orthopyroxenite (Dabie-Shan, China) as monitors for metasomatism and fluid-related trace element transfer in subduction zone peridotite. Earth Planet. Sci. Lett. 249, 173–187.

Malaspina, N., Langenhorst, F., Tumiati, S., Campione, M., Frezzotti, M.L., Poli, S., 2017. The redox budget of crust-derived fluid phases at the slab-mantle interface. Geochim. Cosmochim. Acta 209, 70-84.

Malaspina, N., Scambelluri, M., Poli, S., Van Roermund, H.L.M., Langenhorst, F., 2010. The oxidation state of mantle wedge majoritic garnet websterites metasomatised by C-bearing subduction fluids. Earth Planet. Sci. Lett. 298, 417–426.

Malaspina N, Tumiati S, 2012. The role of C-O-H and oxygen fugacity in subduction-zone garnet peridotites. Eur. J. Mineral. 24, 607–618.

Marschall, H.R., Schumacher, J.C., 2012. Arc magmas sourced from mélange diapirs in subduction zones. Nat. Geosci. 5, 862–867.

McDonough, W.F., Sun, S.S., 1995. The composition of the Earth. Chem. Geol. 120, 223–253.

McLellan, E. L. (1989). Sequential formation of subsolidus and anatectic migmatites in response to thermal evolution, eastern Scotland. J. Geol. 97(2), 165-182.

Milnes, A.G., 1974. Structure of the Pennine Zone (Central Alps): a new working hypothesis. Bulletin of the Geological Society of America. Bull. Geol. Soc. Am. 85, 1727–1732.

Nagel, T.J., 2008. Tertiary subduction, collision and exhumation recorded in the Adula nappe, central Alps. Geol. Soc. London, Spec. Publ. 298, 365–392.

Nimis, P., Trommsdorff, V., 2001. Revised Thermobarometry of Alpe Arami and other Garnet Peridotites from the Central Alps. J. Petrol. 42, 103–115.

Paquin, J., Altherr, R., 2001. New Constraints on the P – T Evolution of the Alpe Arami Garnet Peridotite Body (Central Alps , Switzerland) 42, 1119–1140.

Rampone, E., Morten, L., 2001. Records of Crustal Metasomatism in the Garnet Peridotites of the Ulten Zone (Upper Austroalpine, Eastern Alps). J. Petrol. 42, 207–219.

Rubatto, D., Hermann, J., Berger, A., Engi, M., 2009. Protracted fluid-present melting during Barrovian metamorphism in the Central Alps. Contrib. Mineral. Petrol. 158, 703–722.

Salters, V.J.M., Stracke, A., 2004. Composition of the depleted mantle. Geochem. Geophys. Geosyst. 5(5).

Sapienza, G.T., Scambelluri, M., Braga, R., 2009. Dolomite-bearing orogenic garnet peridotites witness fluid-mediated carbon recycling in a mantle wedge (Ulten Zone, Eastern Alps, Italy). Contrib. Mineral. Petrol. 158, 401–420.

Scambelluri, M., Hermann, J., Morten, L., Rampone, E., 2006. Melt- versus fluid-induced metasomatism in spinel to garnet wedge peridotites (Ulten Zone, Eastern Italian Alps): clues from trace element and Li abundances. Contrib. Mineral. Petrol. 151, 372–394.

Scambelluri, M., Pettke, T., Rampone, E., Godard, M., Reusser, E., 2014. Petrology and Trace Element Budgets of High-pressure Peridotites Indicate Subduction Dehydration of Serpentinized Mantle (Cima di Gagnone, Central Alps, Switzerland). J. Petrol. 55, 459–498.

Scambelluri, M., Pettke, T., van Roermund, H.L.M., 2008. Majoritic garnets monitor deep subduction fluid flow and mantle dynamics. Geology 36, 59.

Schmid, S.M., O.A., P., Froitzheim, N., Schönborn, G., Kissingl, E., 1996. Geophysical-geological transect and tectonic evolution of the Swiss-Italian Alps. Tectonics 15, 1036–1064.

Schmid, S.M., Rück, P., Schreurs, G., 1990. The significance of the Schams nappe for the reconstruction of the paleotectonic and orogenic evolution of the Penninic zone along the NFP 20 East Traverse, in: Pfiffner, A., Heitzmann, P. (Ed.), Deep Structure of the Alps—Results from NFP/PNR 20. Basel: Birkhäuser AG, pp. 263–287.

Schmidt, M.W., Poli, S., 1998. Experimentally based water budgets for dehydrating slabs and consequences for arc magma generation. Earth Planet. Sci. Lett. 163, 361–379.

Schmidt, M.W., Poli, S., 2014. Devolatilization During Subduction. Treatise on Geochemistry: Second Edition. Elsevier Ltd. doi:10.1016/B978-0-08-095975-7.00321-1

Schmidt, M.W., Vielzeuf, D., Auzanneau, E., 2004. Melting and dissolution of subducting crust at high pressures: the key role of white mica. Earth Planet. Sci. Lett. 228, 65–84.

Spandler, C., Pirard, C., 2013. Element recycling from subducting slabs to arc crust: A review. Lithos 170–171, 208–223.

Steinmann, M., Stille, P., 1999. Geochemical evidence for the nature of the crust beneath the eastern North Penninic basin of the Mesozoic Tethys ocean. Geol. Rundschau 87, 633–643.

Stucki, A., Rubatto, D., Trommsdorff, V., 2003. Mesozoic ophiolite relics in the Southern Steep Belt of the Central Alps. Schweiz. Mineral. Petrogr. Mitt. 83, 285–299.

Syracuse, E.M., van Keken, P.E., Abers, G.A., Suetsugu, D., Bina, C., Inoue, T., Wiens, D., Jellinek, M., 2010. The global range of subduction zone thermal models. Phys. Earth Planet. Inter. 183, 73–90.

Tiraboschi, C., Tumiati, S., Sverjensky, D., Pettke, T., Ulmer, P., Poli, S., 2018. Experimental determination of magnesia and silica solubilities in graphite-saturated and redox-buffered high-pressure COH fluids in equilibrium with forsterite + enstatite and magnesite + enstatite. Contrib. Mineral. Petrol. 173.

Todd, C.S., Engi, M., 1997. No Title. Metamorph. F. gradients Cent. Alps. J. Metamorph. Geol. 15, 513–530.

Tommasi, A., Langone, A., Padrón-Navarta, J. A., Zanetti, A., Vauchez, A., 2017. Hydrous melts weaken the mantle, crystallization of pargasite and phlogopite does not: Insights from a petrostructural study of the Finero peridotites, southern Alps. Earth Planet. Sci. Lett., 477, 59-72.

Trommsdorff, V., Hermann, J., Muntener, O., Pfiffner, M., Risold, A.C., 2000. Geodynamic cycles of subcontinental lithosphere in the Central Alps and the Arami enigma. J. Geodyn. 30, 77–92.

Tumiati, S., Fumagalli, P., Tiraboschi, C., Poli, S., 2013. An Experimental Study on COH-bearing Peridotite up to 3.2 GPa and Implications for Crust-Mantle Recycling. J. Petrol. 54, 453–479.

Tumiati, S., Godard, G., Martin, S., Klötzli, U., Monticelli, D., 2007. Fluid-controlled crustal metasomatism within a high-pressure subducted mélange (Mt. Hochwart, Eastern Italian Alps). Lithos 94, 148–167.

Tumiati, S., Godard, G., Martin, S., Nimis, P., Mair, V., Boyer, B., 2005. Dissakisite-(La) from the Ulten zone peridotite (Italian Eastern Alps): A new end-member of the epidote group. Am. Mineral. 90, 1177–1185.

Tumiati, S., Thöni, M., Nimis, P., Martin, S., Mair, V., 2003. Mantle–crust interactions during Variscan subduction in the Eastern Alps (Nonsberg–Ulten zone): geochronology and new petrological constraints. Earth Planet. Sci. Lett. 210, 509–526.

Tumiati, S., Zanchetta, S., Pellegrino, L., Ferrario, C., Casartelli, S., Malaspina, N., 2018. Granulite-facies overprint in garnet peridotites and kyanite eclogites of Monte Duria (Central Alps, Italy): Clues from srilankite- and sapphirine-bearing symplectites. J. Petrol. 59.

Van Roermund, H. van, Carswell, D., Drury, M.R., Heijboer, T.C., 2002. Microdiamonds in a megacrystic garnet websterite pod from Bardane on the island of Fjørtoft, western Norway: evidence for diamond formation in mantle rocks during. Geology 30, 959.

Wang, L., Kusky, T. M., Polat, A., Wang, S., Jiang, X., Zong, K., Wang, J., Deng, H., Fu, J. (2014). Partial melting of deeply subducted eclogite from the Sulu orogen in China. Nature communications, 5, 5604.

Figure captions

Fig. 1

(a) Tectonic scheme of the Adula-Cima Lunga Nappes modified after Burri et al. (2005). (b) Detailed geological scheme of the Monte Duria area with the locations of Mt. Duria and Borgo outcrops modified from Tumiati et al. (2018). At: Antigorio; Mg: Maggia; Sm: Simano; LL: Leventina-Lucomagno; Tb: Tambò; Su: Suretta; SSB: Southern Steep Belt.

Fig. 2

(a) Borgo outcrop. PDT: retrogressed garnet peridotite; AG: amphibole-bearing migmatites; ME: mafic eclogites; E: kyanite eclogites; HAE: high-Al_2O_3 rim between kyanite eclogites and host amphibole-bearing migmatites. (b) Detailed geological map of the Borgo outcrop (from Tumiati et al., 2018) with samples locations.

Fig. 3

Structures of ultramafic rocks of Mt. Duria and Borgo. (a) Garnet peridotite lens on the southern ridge of Monte Duria. (b) Detail of garnet layering transposed by a secondary chlorite foliation in garnet peridotite from Monte Duria. (c) Chlorite-bearing pseudomorphs replacing garnets in chlorite peridotite of Borgo. (d) Retrogressed garnet layering transposed by a younger chlorite foliation in chlorite peridotite of Borgo.

Fig. 4

Lithologies and structures of ultramafic and mafic rocks of Borgo. (a) Tremolitite boudin within the chlorite peridotite, with samples location. (b) Detail of tremolitite boudin with garnet layering wrapping around the boudins and flowing into the boudins neck. (c) Garnet layering wrapping the tremolitite boudin and Phl_3 + Chl +Tr + Tc pseudomorphs replacing garnet in tremolitites. (d) leucosomes and melanosomes in amphibole-bearing migmatites; e) lobes and cusps structures in amphibole-bearing migmatites.

Fig. 5

Photomicrographs and back-scattered electron (BSE) images of peridotites and tremolitites. (a) Cross polarised light image of Mt. Duria garnet peridotite B3A showing garnet porphyroclasts and coarse orthopyroxene (Opx_1) and clinopyroxene (Cpx_1) and amphibole (Amp_1) in a matrix of finer grained matrix; (b) Cross polarised light image of neoblastic orthopyroxene (Opx_2), clinopyroxene (Cpx_2) and spinel (Sp_2) in sample B3A. (c) Plane polarised light image of porphyroblastic orthopyroxene (Opx_{Porph}), phlogopite (Phl_{Porph}) and amphibole (Amp_{Porph}) statically growing at the expenses of relict olivine and orthopyroxene in chlorite peridotite DB113 from Borgo. (d) BSE image of dolomite in textural equilibrium with olivine and chlorite (Chl_1) in sample DB113. (d) BSE image of relict Mg-hornblende overgrown by tremolite and minor chlorite (Chl_3) in tremolitite DB148 from Borgo. (f) Plane polarised light image of phlogopite (Phl_3) + Chl_3 + Tr + Tlc after garnet in tremolitite DB179 from Borgo.

Fig. 6

BSE images of eclogites from Borgo. (a) Quartz porphyroblasts surrounded by Cpx_M + Kfs_M coronas and K-feldspar porphyroblasts surrounded by symplectitic clinopyroxene (Cpx_2) in mafic eclogite D6. (b) Zoisite porphyroblast surrounded by tiny, bright allanite crystals in mafic eclogite D6. (c) Melt pocket of recrystallised Cpx_M + Kfs_M around relict quartz and Pl_2+Cpx_2+Amp_2 symplectite after omphacite in high-Al_2O_3 eclogite D9. (d) Melt pocket of recrystallised Kfs_M + Pl_M + Qz_M + Cpx_M around relict quartz in high-Al_2O_3 eclogite D9. (d) Pl_2 + Amp_2 symplectite replacing garnet in Na-rich Pl_2 + Amp_2 + Cpx_2 symplectite after omphacite in amphibole-bearing migmatite D5. (f) Pl_2 + Cpx_2 + Amp_2 symplectite after omphacite in amphibole-bearing migmatite D5.

Fig. 7

Mg# versus Ni (ppm) plot (a) and CaO versus Al_2O_3 wt.% concentrations (b) of peridotites from Mt. Duria and tremolitite and eclogites from Borgo (data from Table 2) compared with Depleted Mantle (Salters and Stracke, 2004), average N-MORB (Gale et al., 2013), average composition of Mean Upper Crust, Mean Shallow Gabbro and Mean Lower Gabbro (Gillis et al., 2014), peridotites from Ulten Zone (UZ; Tumiati et al., 2003), Cima di Gagnone (CdG; Scambelluri et al., 2014), Alpe Arami (AA; Ernst, 1978) and peridotite and Mg-gabbro from the Bellinzona-Dascio Zone (BDZ; Stucki et al., 2003). The dashed black line separates mafic compositions on the left form the ultramafic compositions on the right (modified after Malaspina et al., 2006).

Fig. 8

Primitive Mantle normalised REE and other trace element patterns of the investigated samples (data from Table 2). Elements are presented in order of increasing compatibility (left to right) during melting in the upper mantle (Gale et al., 2013). Normalising values are from McDonough and Sun (1995). (a) and (b) trace elements pattern of A2C2 and B3A garnet peridotites from Monte Duria, compared with the reference Depleted Mantle (blue solid line DM; Salters and Stracke, 2004), garnet peridotites from Cima di Gagnone (grey area CdG; Scambelluri et al., 2014), garnet peridotites from Ulten Zone (pink area UZ; Scambelluri et al., 2006 and Tumiati et al., 2007). (c) and (d) trace elements pattern of tremolitite DB151. (e) and (f) trace elements pattern of D6, D9, B5A eclogites and interstitial Cpx_M + Kfs_M pocket aggregate in high-Al_2O_3 eclogite D9 compared with average N-MORB pattern (solid grey line; Gale et al., 2013), Mg-gabbro from Bellinzona-Dascio Zone (light grey area BDZ; Stucki et al., 2003) and the trace element pattern of allanite from eclogite D6.

Fig. 9

(a) Compositional variation of clinopyroxenes (octahedral Al versus Na) in garnet peridotites from Mt. Duria and chlorite peridotites from Borgo. (b) Al versus Si content of porphyroclastic, neoblastic and symplectitic orthopyroxenes of garnet peridotites from Mt. Duria and porphyroblastic metasomatic orthopyroxene in chlorite peridotite from Borgo. (c) and (d) Compositional variations of amphiboles from garnet and chlorite peridotites. Tetrahedral aluminium (Al^{IV}) is plotted with respect to total Na and octahedral aluminium (Al^{VI}); Ts = tschermakite, Ed = edenite, Pg = pargasite, Tr = tremolite.

Fig. 10

Octahedral Al versus Na compositional variation of clinopyroxenes (a) and tetrahedral aluminium versus total Na and octahedral aluminium compositional variation of amphiboles in eclogites boudins from Borgo. Abbreviations same as in Figure 9.

Fig. 11

Primitive mantle normalised REE and other trace elements patterns of (a) and (b) porphyroclastic garnets, clinopyroxenes and amphiboles of garnet peridotites from Mt. Duria; (c) and (d) porphyroblastic metasomatic amphibole of chlorite peridotites from Borgo; (e) and (f) relict hornblendes and tremolites from tremolitite boudins at the contact between chlorite peridotite and amphibole-bearing migmatites at Borgo.

Fig. 12

Primitive mantle normalised REE and other trace elements patterns of garnets (a) and (b), zoisite (c), allanite (d) and amphiboles (e) and (f) from all eclogite types at Borgo. The different colour labels of allanite in (d) indicate different point analyses of the same samples because of the scattered normalised concentrations of MREE and HREE.

Fig. 13

Peak P-T conditions of mafic (red square) and ultramafic (green square) rocks in the Monte Duria area (from Tumiati et al., 2018). In the P-T space are reported: i) basalt wet solidus (Schmidt and Poli, 1998); ii) zoisite and amphibole-out curves (Schmidt and Poli, 1998); iii) phengite dehydration melting curves in basalt ((1) Hermann and Green, 2001; (2) Liu et al., 2009); iv) basalt dry solidus (Lambert and Wyllie, 1972); v) chlorite-out curve in the peridotite system (Fumagalli and Poli, 2005); vi) top slab geotherms of warm subduction zones (orange field; Syracuse et al., 2010) and of cold subduction zones (grey field, Arcay et al., 2007). Note that the peak conditions of the coupled eclogites and garnet peridotites overlap the "warm" subduction P-T path suggesting that Borgo eclogites can be considered as a proxy for partial flush melting of a mafic crust in a thermal regime characterised by a low angle subduction zone.

Fig. 14

a) log aH$_2$O–X diagram calculated at fixed P = 3 GPa and T = 750°C for garnet websterite forming after the melt-peridotite reaction. X = 0 corresponds to garnet peridotite (A2C2, Tab. 2), while X = 1 corresponds to the bulk of leucosome pockets composition (D9, Fig. S-3, Tab. 2). Dashed lines and corresponding black numbers in the lower part of the section are the isomodes of clinopyroxene (vol.%) increasing from peridotite to leucosome composition, whereas orthopyroxene increases from 19 to 40 vol.% in the range $0<X<0.45$ and decreases from 37 to 2 vol.% in the range $0.5<X<1$. b) T-X diagram calculated at H_2O saturated condition of the websterites forming after the reaction between peridotite and eclogite leucosome in the range of interest ($0<X<0.45$) at 0.7 GPa, representing the beginning of retrogression. Dashed grey lines and corresponding black numbers are the isopleths of the tremolite molar content in the amphibole solid solution (mol.%).

Fig.15

Conceptual model for garnet websterite formation at the slab-mantle interface in a deformation regime during subduction (not to scale). See text for explanation. Isotherms in the inset are relative to warm subduction environments (Peacock and Wang, 1999).

Tab. 1

Mineral assemblages stable at peak, decompression, low pressure and high-temperature and the retrogression stages, reconstructed from microstructures of Monte Duria peridotites and eclogites.

Tab. 2

Major (oxide wt.%) and trace (ppm) element compositions of whole-rocks of peridotites, eclogites, metasomatic layer and migmatite leucosome from Monte Duria area.

Tab. 3

Representative WDS microprobe analyses (oxide wt.%) and reconstructed formulae of garnet (Grt), clinopyroxene (Cpx, Omp), orthopyroxene (Opx), olivine (Ol), amphiboles (Amp, Hbl, Tr), plagioclase (Pl), K-feldspar (Kfs) and biotite (Bt) in selected samples of peridotites and eclogites from Monte Duria area.

Tab. 4

Trace element composition (ppm) of representative minerals of selected samples of peridotites and eclogites from Monte Duria area.

High pressure melting of eclogite and metasomatism of garnet peridotites from Duria Area (Central Alps, N Italy): a proxy for melt-rock reaction during subduction

Luca Pellegrino[1], Nadia Malaspina[1*], Stefano Zanchetta[1], Antonio Langone[3], Simone Tumiati[2]

[1*] Dipartimento di Scienze dell'Ambiente e della Terra, Università degli Studi di Milano - Bicocca, Piazza della Scienza 4, 20126 Milano, Italy (*nadia.malaspina@unimib.it; ph:+39 0264482042; fax: +39 0264482073)

[2] Dipartimento di Scienze della Terra, Università degli Studi di Milano, via Mangiagalli 34, 20133 Milano, Italy

[3] Istituto di Geoscienze e Georisorse-C.N.R. U.O.S. of Pavia, Via Ferrata 1, 27100 Pavia, Italy

Supplementary material

Analytical methods and thermodynamic modelling

Major and trace elements whole-rock analyses were performed by inductively-coupled plasma mass spectrometry (ICP-MS) and LECO combustion (total C, S) at Bureau Veritas ACME Mineral Laboratories, Canada. Results are reported in Table 2.

Major elements composition of minerals was determined using a JEOL 8200 wavelength dispersive electron microprobe at the Department of Earth Sciences of the University of Milano. Quantitative analyses (Tab. 3) were performed using 15 kV accelerating potential, 5 nA sample current and 1 µm beam diameter. Standards used were omphacite (Na), grossular (Ca, Al and Si), fayalite (Fe), olivine (Mg), orthoclase (K), rhodonite (Mn), ilmenite (Ti), niccolite (Ni), pure Cr (Cr) and zircon (Zr, Hf). A counting time of 30 s was applied for all elements.

Intensity X-ray maps were standardized to concentration maps of oxide weight percentage using spot analyses as internal standard. X-ray maps were processed using XMapTools 2.2.1 (Lanari et al., 2014).

Trace elements composition of minerals was determined using laser ablation inductively coupled plasma mass spectrometry (LA-ICP-MS) at the CNR–IGG–UOS of Pavia. The instrument couples a 213 nm Nd:YAG laser microprobe (NewWave Research) to a quadrupole ICP-MS system (DRCe from PerkinElmer). Trace elements analyses on minerals were performed using 55 µm-sized spot with a fluence of 7.0÷8.0 J/cm^2. The smallest crystals were analysed using 15 µm-sized spot and a fluence of 4 J/cm^2. NIST610 was used as external standard whereas Ca, Si and Al were used as internal standard depending on the analysed minerals. During each analytical session the USGS reference sample BCR2 was analysed for a quality control. The trace elements compositions of analysed minerals are listed in Table 4.

The thermodynamic modelling was performed with the software package Perple_X (http://www.perplex.ethz.ch; Connolly, 2005), using the thermodynamic database of Holland and Powell (1998) revised in 2002 (hp02ver.dat), and the following solution models described by Holland and Powell (1998) (HP), Holland and Powell (2003) (I1, HP and C1) and Dale et al. (2000) (D): Gt(HP) for garnet, Opx(HP) for orthopyroxene, O(HP) for olivine, Omph(HP) for Ca-Na clinopyroxene, Chl(HP) for chlorite, Sp(HP) for spinel, Pheng(HP) for white mica, Bio(HP) for phlogopite, Pl(I1, HP) + OrFsp(C1) for ternary feldspars, Ca-Amp(D) for calcic amphibole. The water equation of state was taken from Holland and Powell (1998).

Mineral abbreviations are from Whitney and Evans (2009).

Additional Figures

Fig. S-1

Borgo outcrop: (a) shear zone defining the contact between migmatitic gneiss and amphibole-bearing migmatite; (b) tremolite-rich metasomatic layer infiltrating the retrogressed garnet peridotite at the contact with amphibole-bearing migmatite.

Fig. S-2 (a) Plane polarised light (PPL) image of chlorite-bearing pseudomorph after garnet surrounded by amphibole + spinel symplectite in sample DB165. (b, c) Close inspection of Chl1 after garnet showing the destabilisation products of Chl_1 at LP-(U)HT retrogression formed by orthopyroxene + spine. (d) Cross polarised light image (XPL) of chlorite peridotite C2A. The chlorite (Chl_3) + amphibole (Amp_3) foliation post-dates the recrystallized olivine + orthopyroxene (Opx_2) + clinopyroxene (Cpx_2) + amphibole (Amp_2) + spinel (Spl_2) peridotite matrix.

Fig. S-3 Back-scattered electron (BSE) image (a) and X-ray maps of SiO_2 (b) CaO (c) and K_2O (d) concentrations of melt pocket of recrystallised Cpx_M + Kfs_M around relict quartz and Pl_2+Cpx_2+Amp_2 symplectite after omphacite in high-Al_2O_3 eclogite D9.

Fig. S-4 BSE image (a) and X-ray maps of SiO_2 (b) CaO (c) and K_2O (d) concentrations of melt pocket of recrystallised Kfs_M + Pl_M + Qz_M + Cpx_M around relict quartz in high-Al_2O_3 eclogite D9

References

Connolly, J.A.D., 2005. Computation of phase equilibria by linear programming: A tool for geodynamic modeling and its application to subduction zone decarbonation. Earth Planet. Sci. Lett. 236, 524–541.

Dale, J., Holland, T. J. B., Powell, R., 2000. Hornblende–garnet–plagioclase thermobarometry: a nat- ural assemblage calibration of the thermodynamics of horn- blende. Contrib. Mineral. Petrol. 140, 353–362.

Holland, T.J.B., Powell, R., 1998. An internally consistent thermodynamic data set for phases pf petrological interest. J. Metamorph. Geol. 16, 309–343.

Holland, T., Powell, R., 2003. Activity–composition relations for phases in petrological cal- culations: an asymmetric multicomponent formulation. Contrib. Mineral. Petrol. 145, 492–501.

Lanari, P., Vidal, O., De Andrade, V., Dubacq, B., Lewin, E., Grosch, E.G., Schwartz, S., 2014. XMapTools: A MATLAB©-based program for electron microprobe X-ray image pro- cessing and geothermobarometry. Computers & Geosciences 62, 227–240

Whitney, D.L., Evans, B.W., 2009. Abbreviations for names of rock-forming minerals. Am. Mineral. 95, 185–187.

Figure 1

Click here to download high resolution image

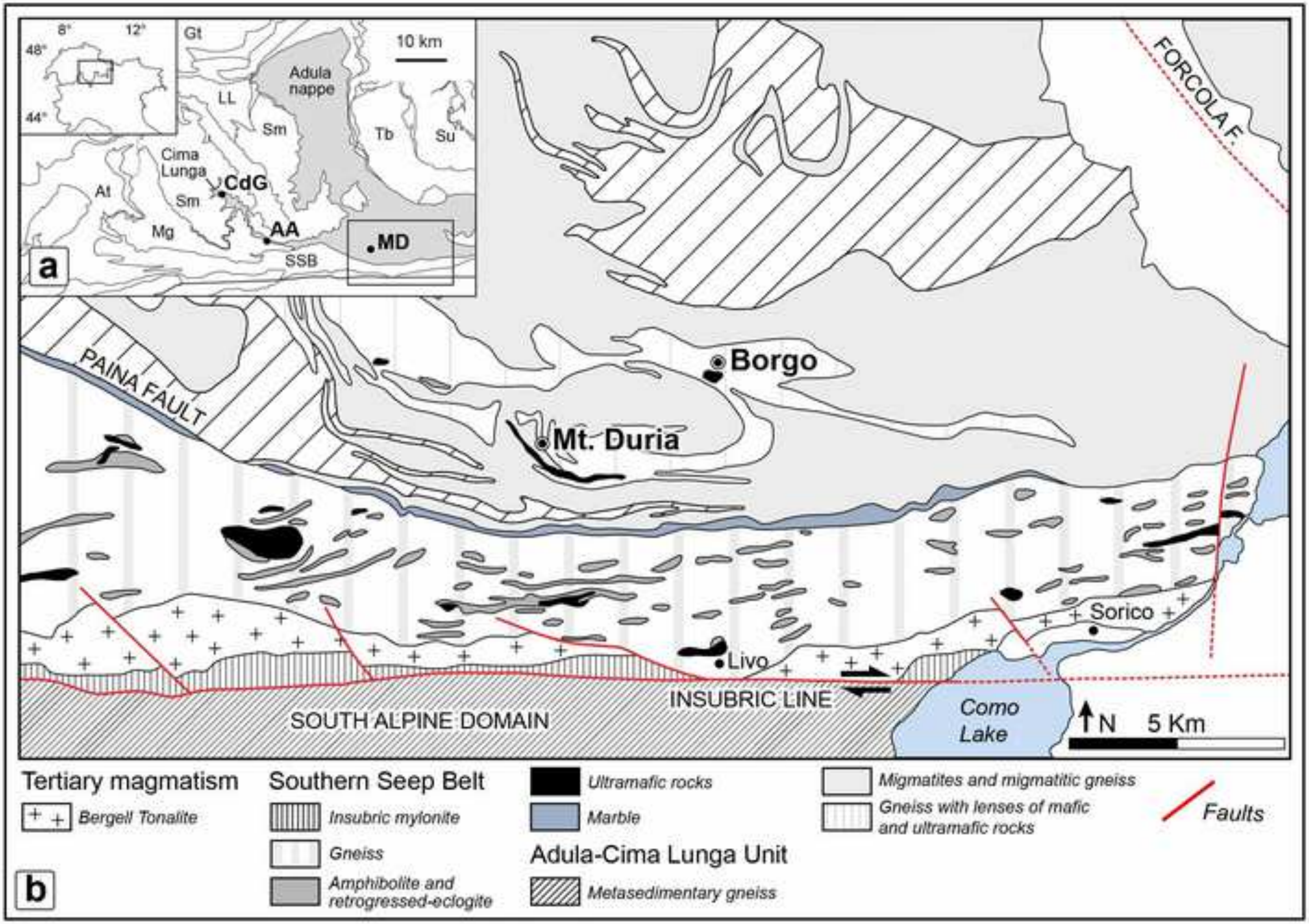

Figure 2

Click here to download high resolution image

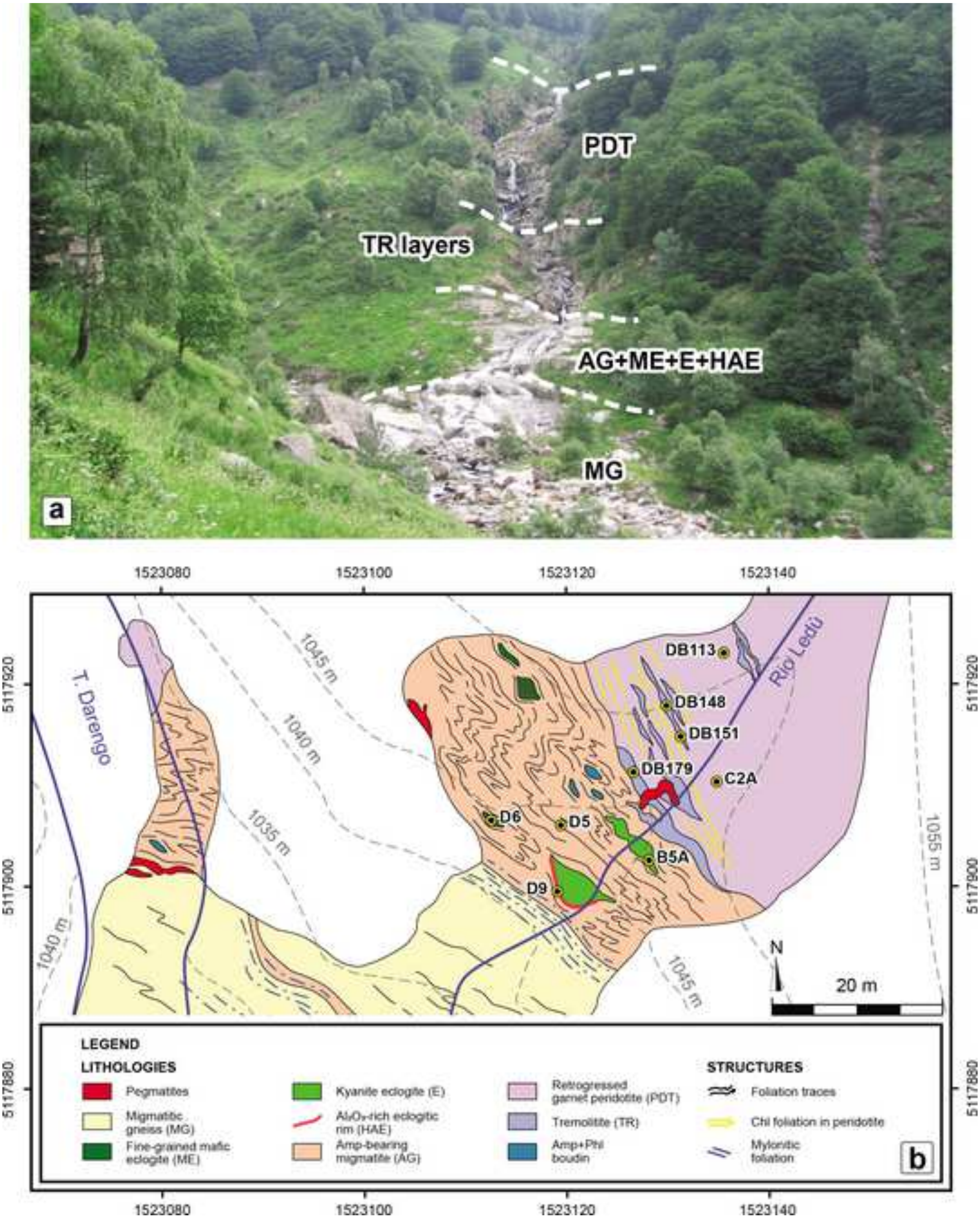

Figure 3

Click here to download high resolution image

Figure 4
Click here to download high resolution image

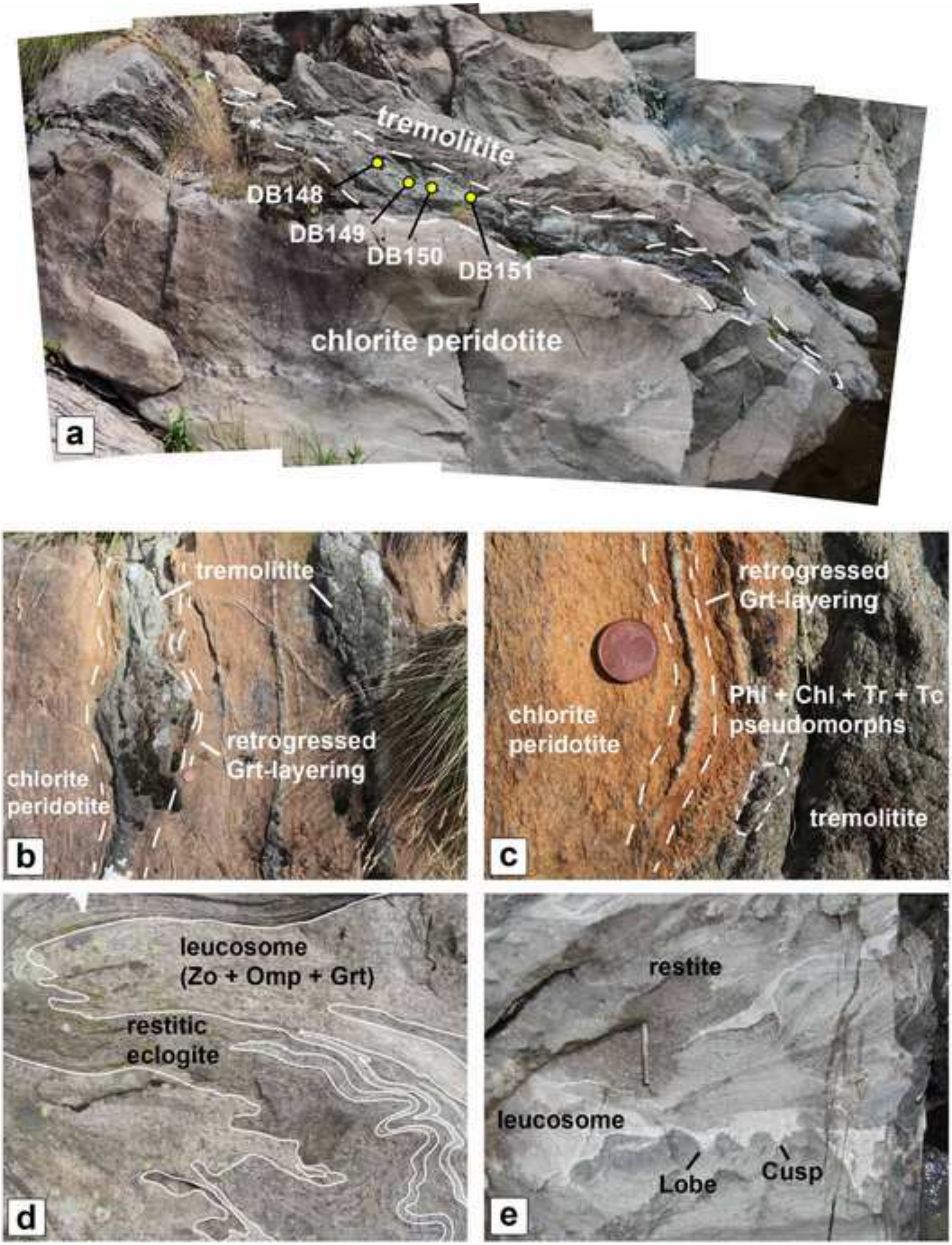

Figure 5
Click here to download high resolution image

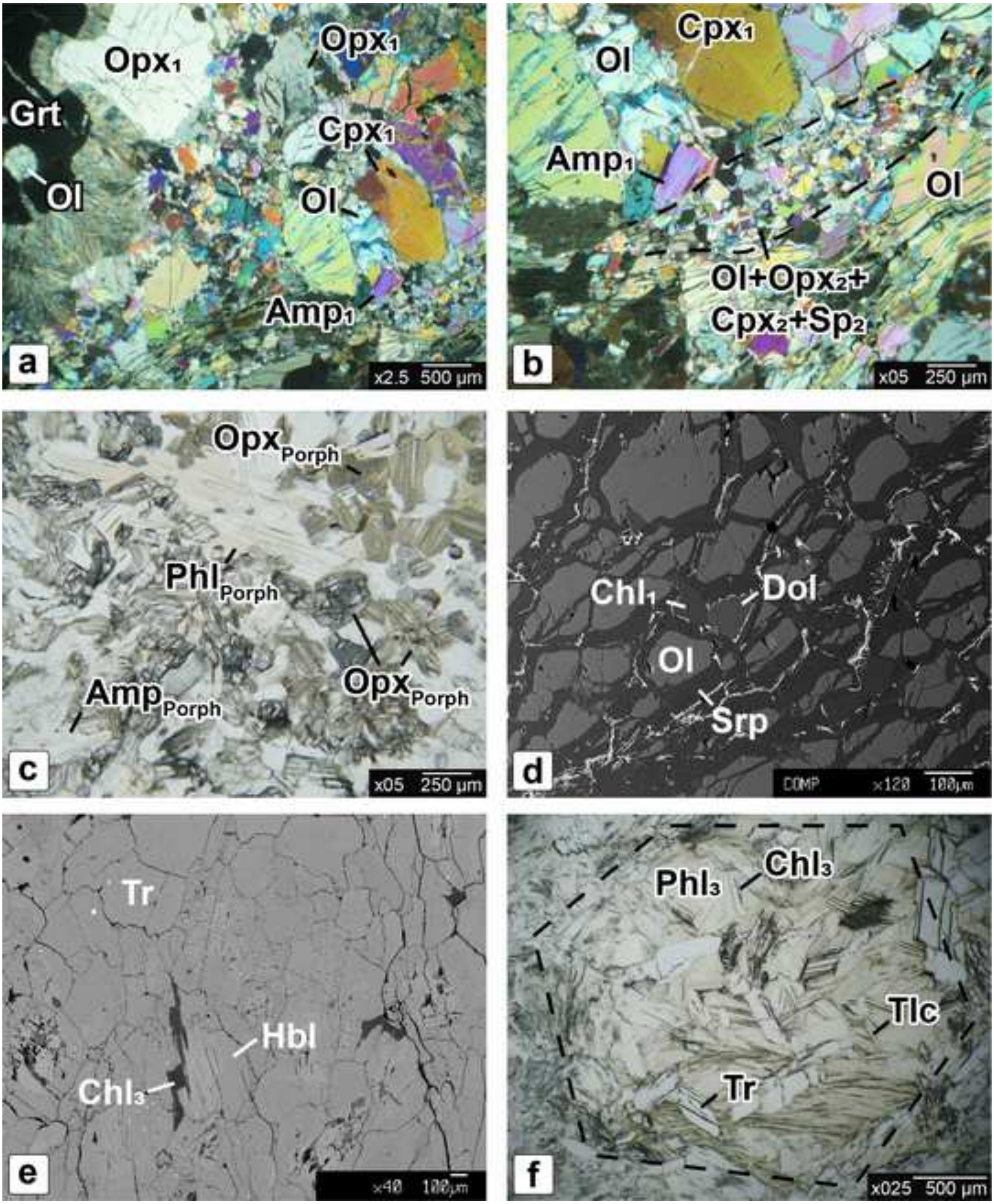

Figure 6
Click here to download high resolution image

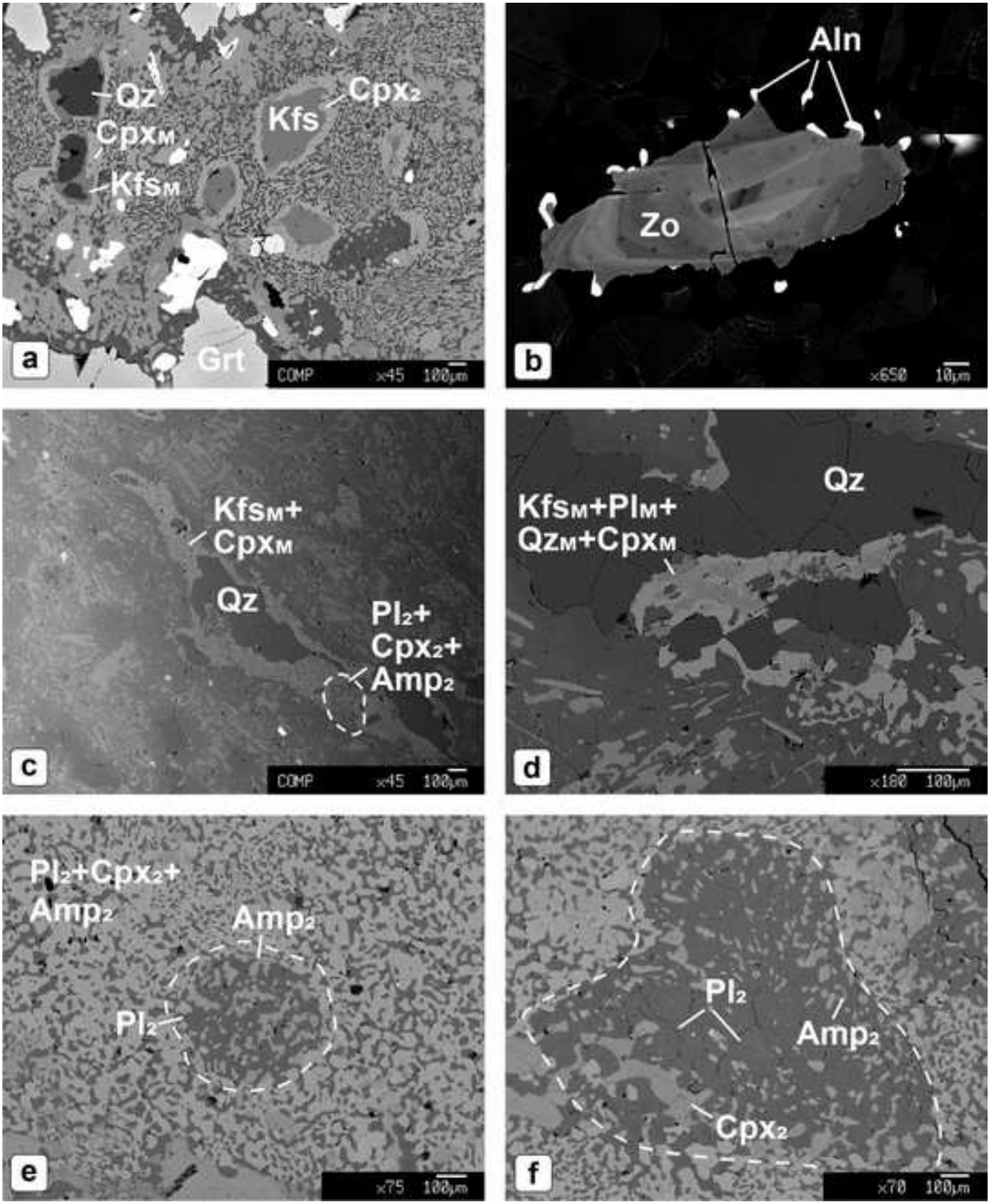

Figure 7
Click here to download high resolution image

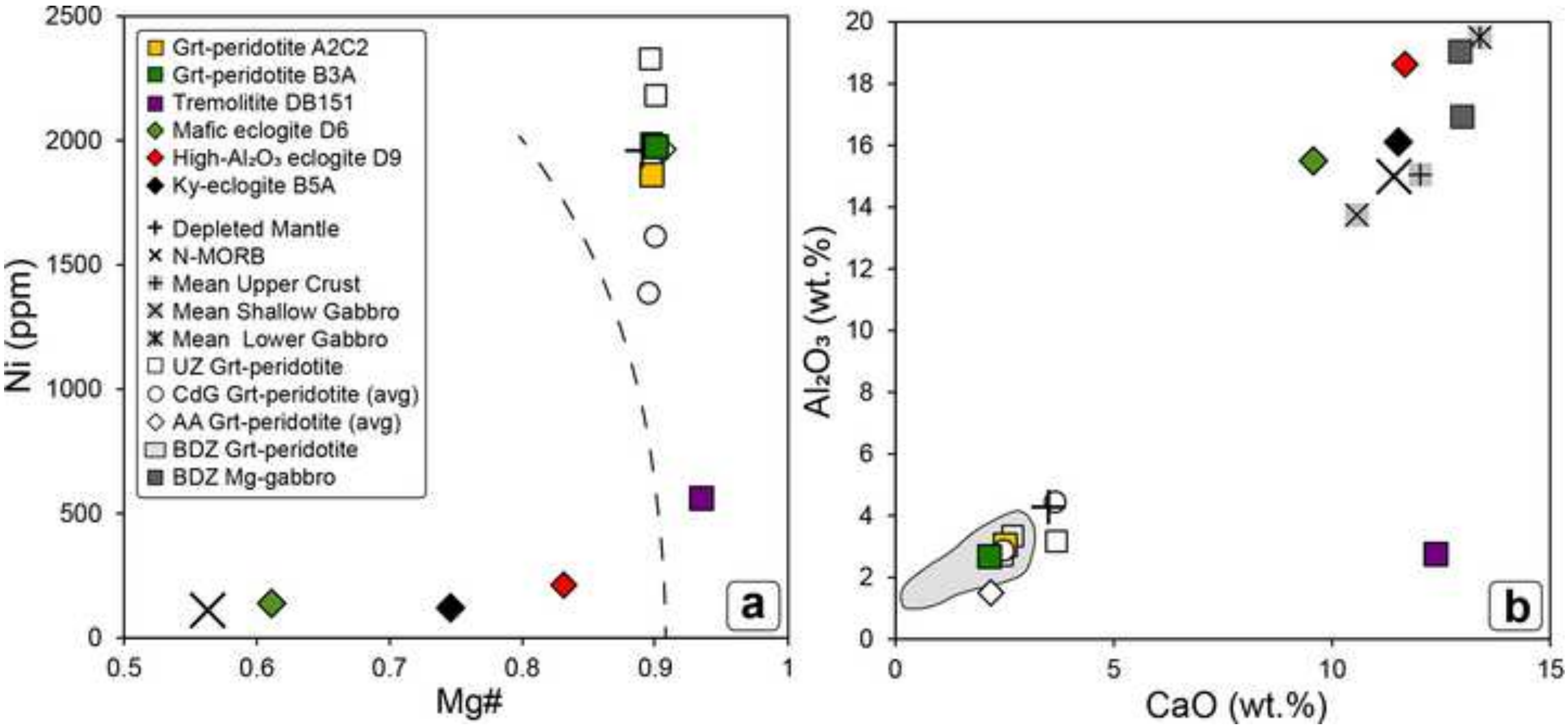

Figure 8
Click here to download high resolution image

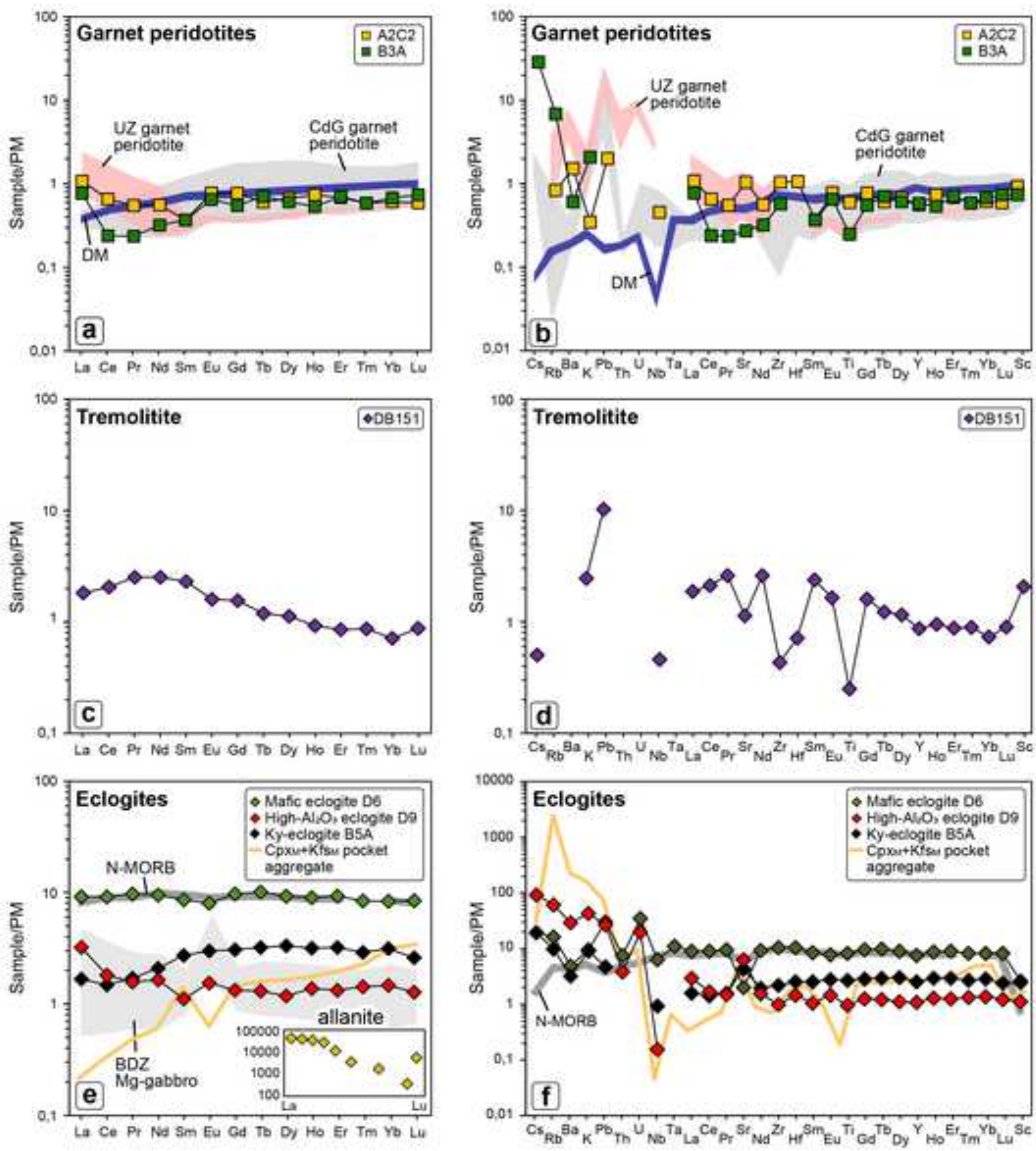

Figure 9
Click here to download high resolution image

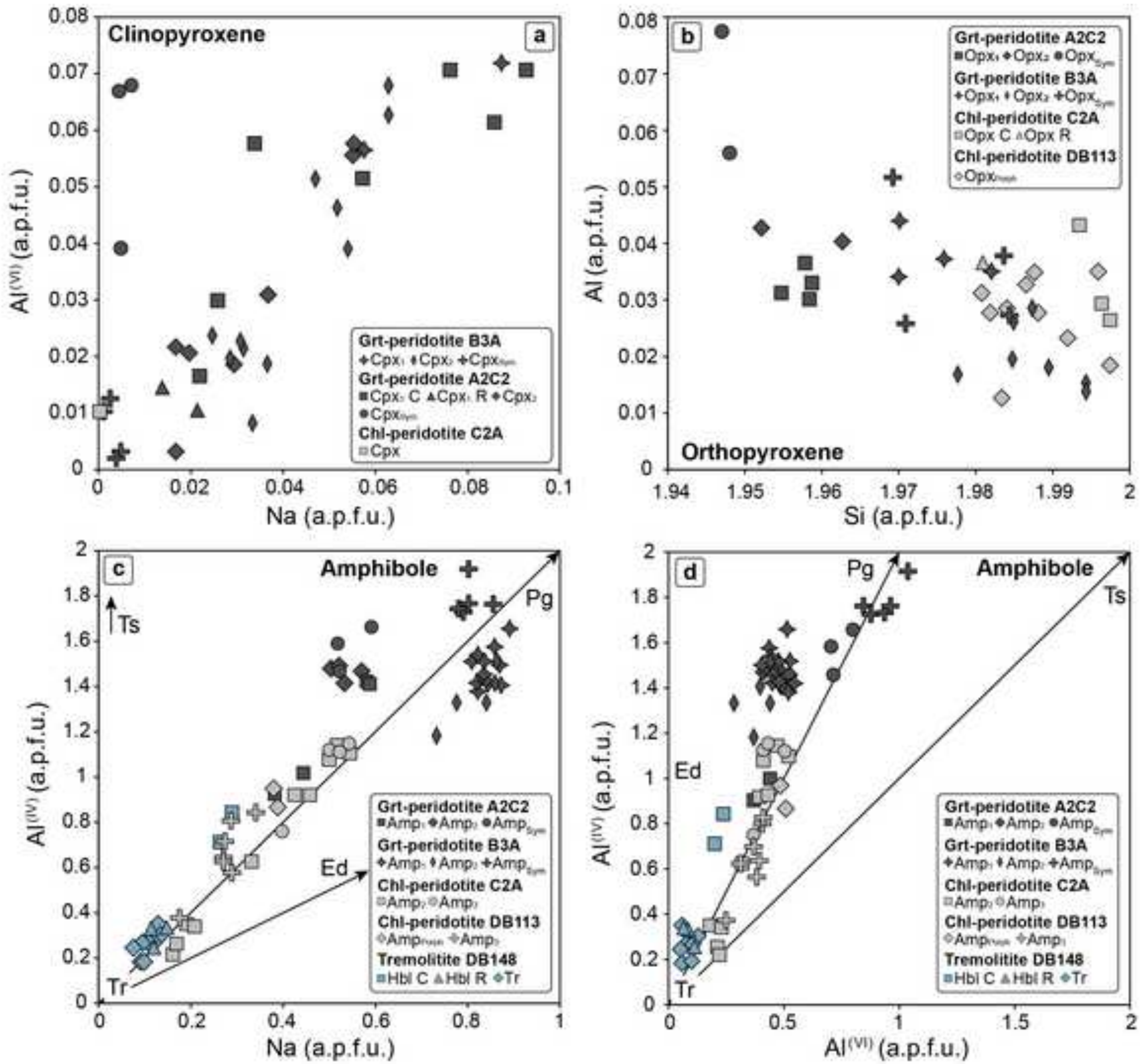

Figure 10

Click here to download high resolution image

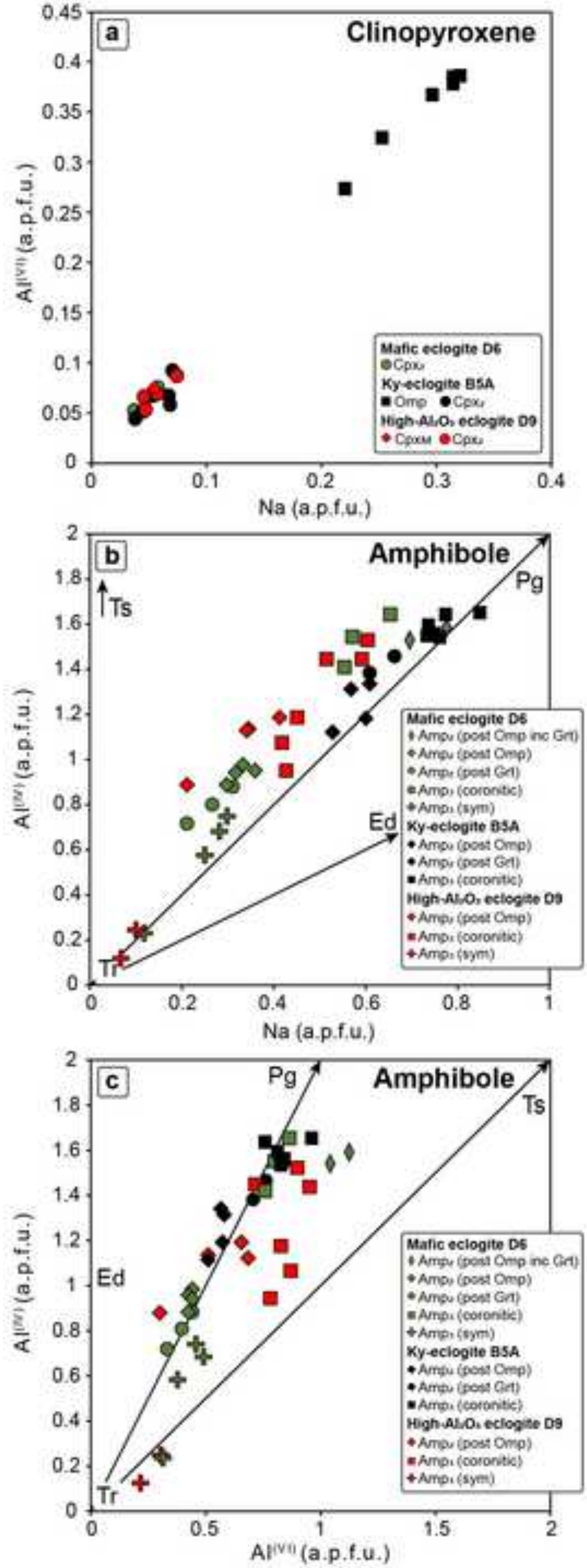

Figure 11
Click here to download high resolution image

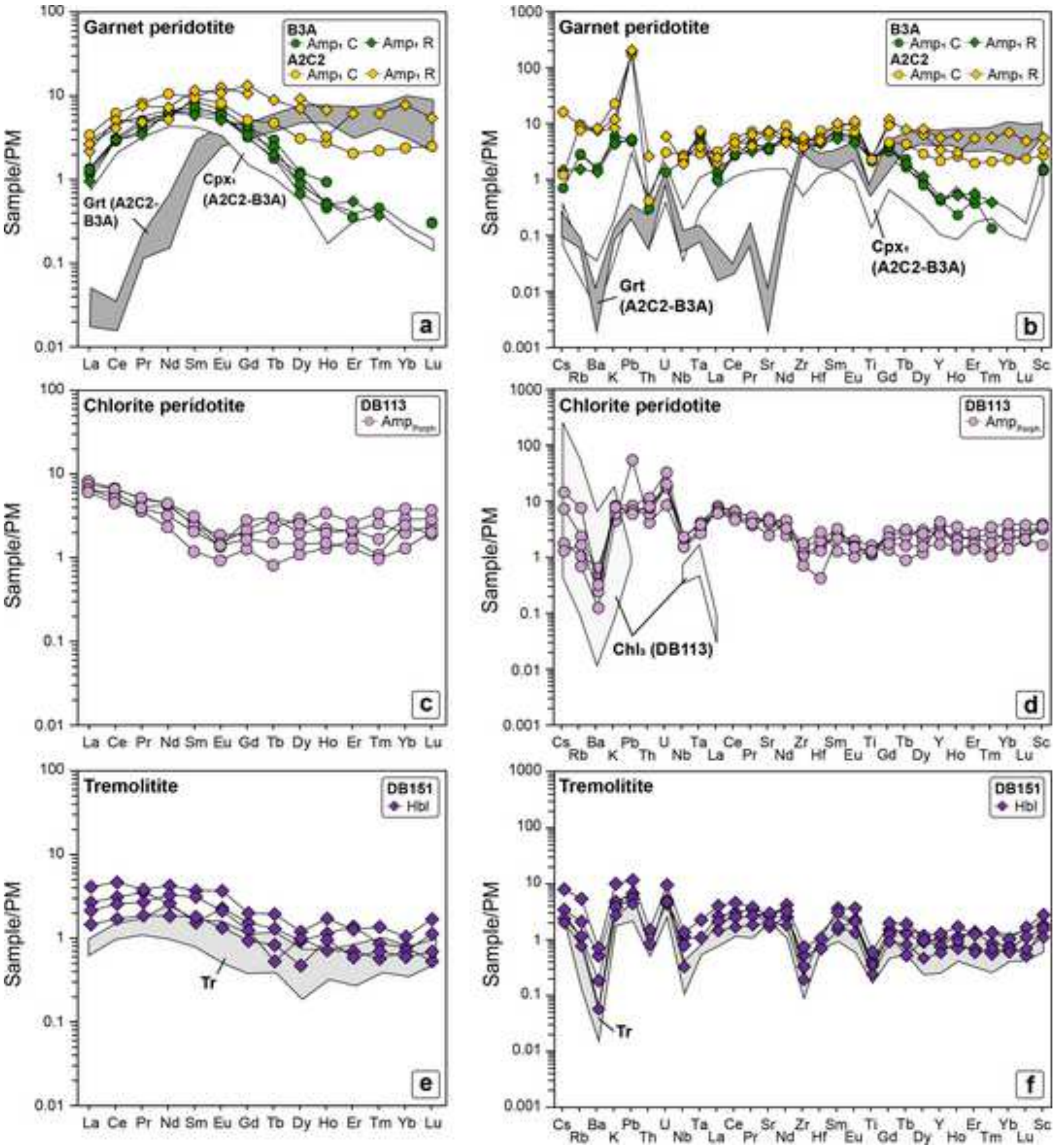

Figure 12

Click here to download high resolution image

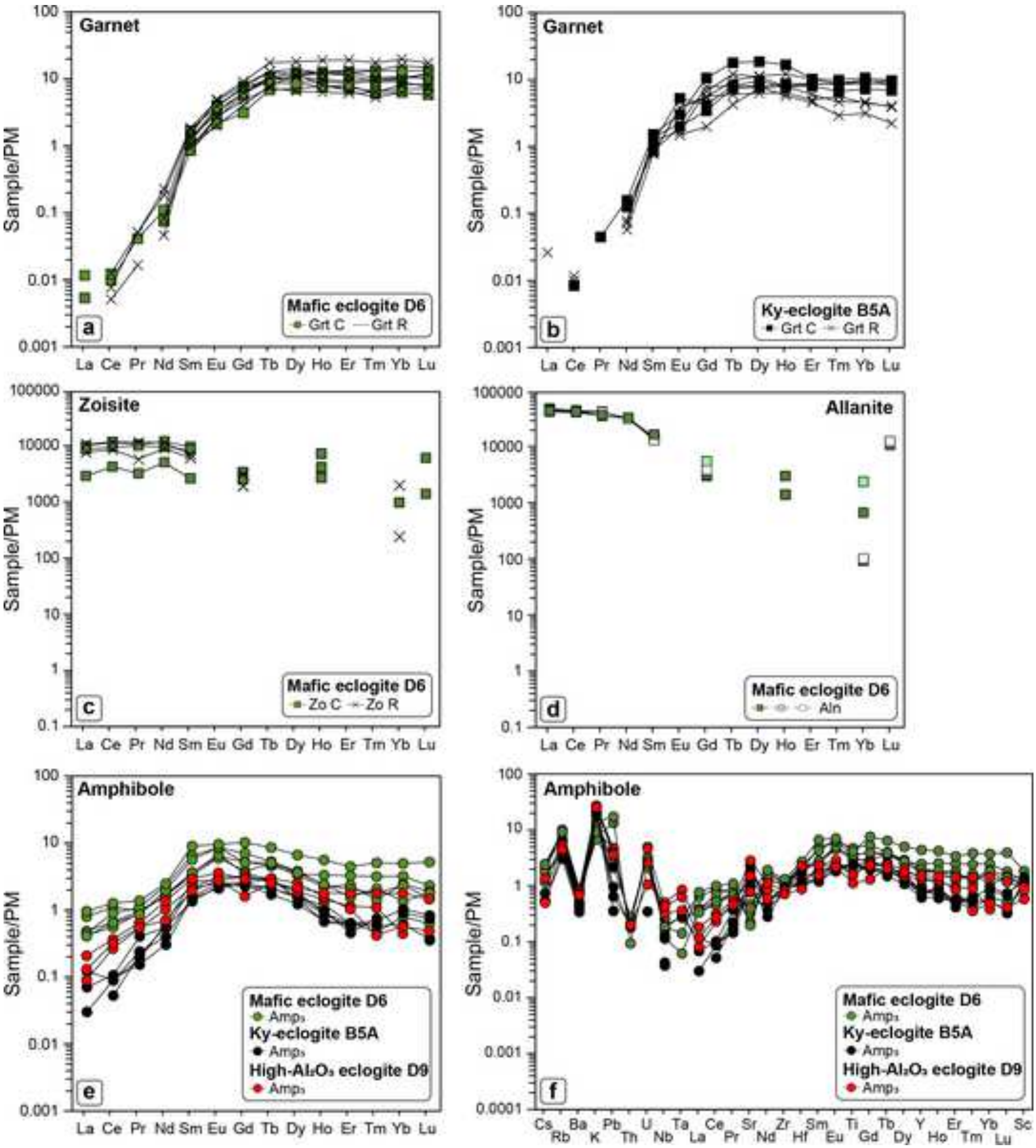

Figure 13
Click here to download high resolution image

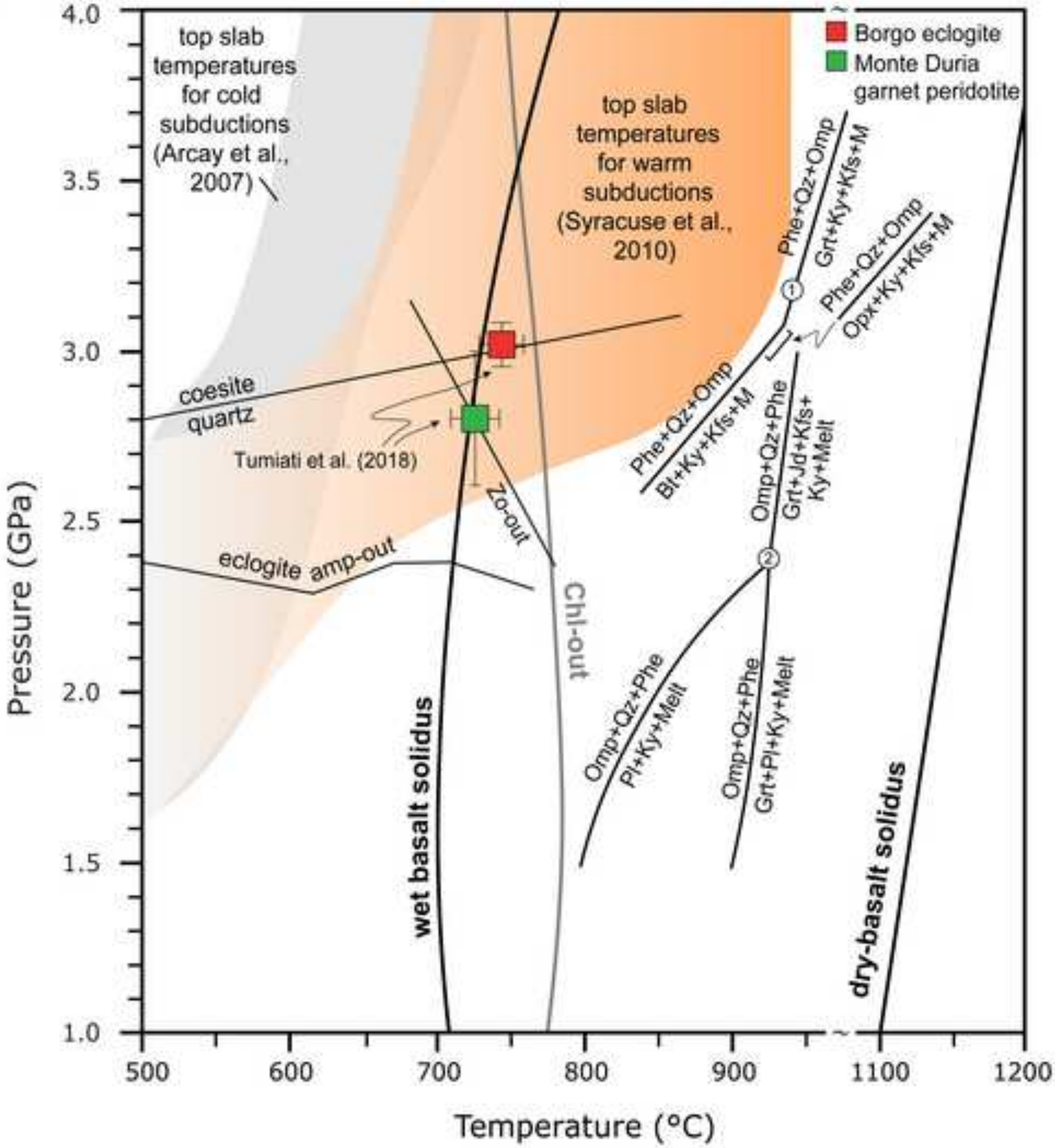

Figure 14

Click here to download high resolution image

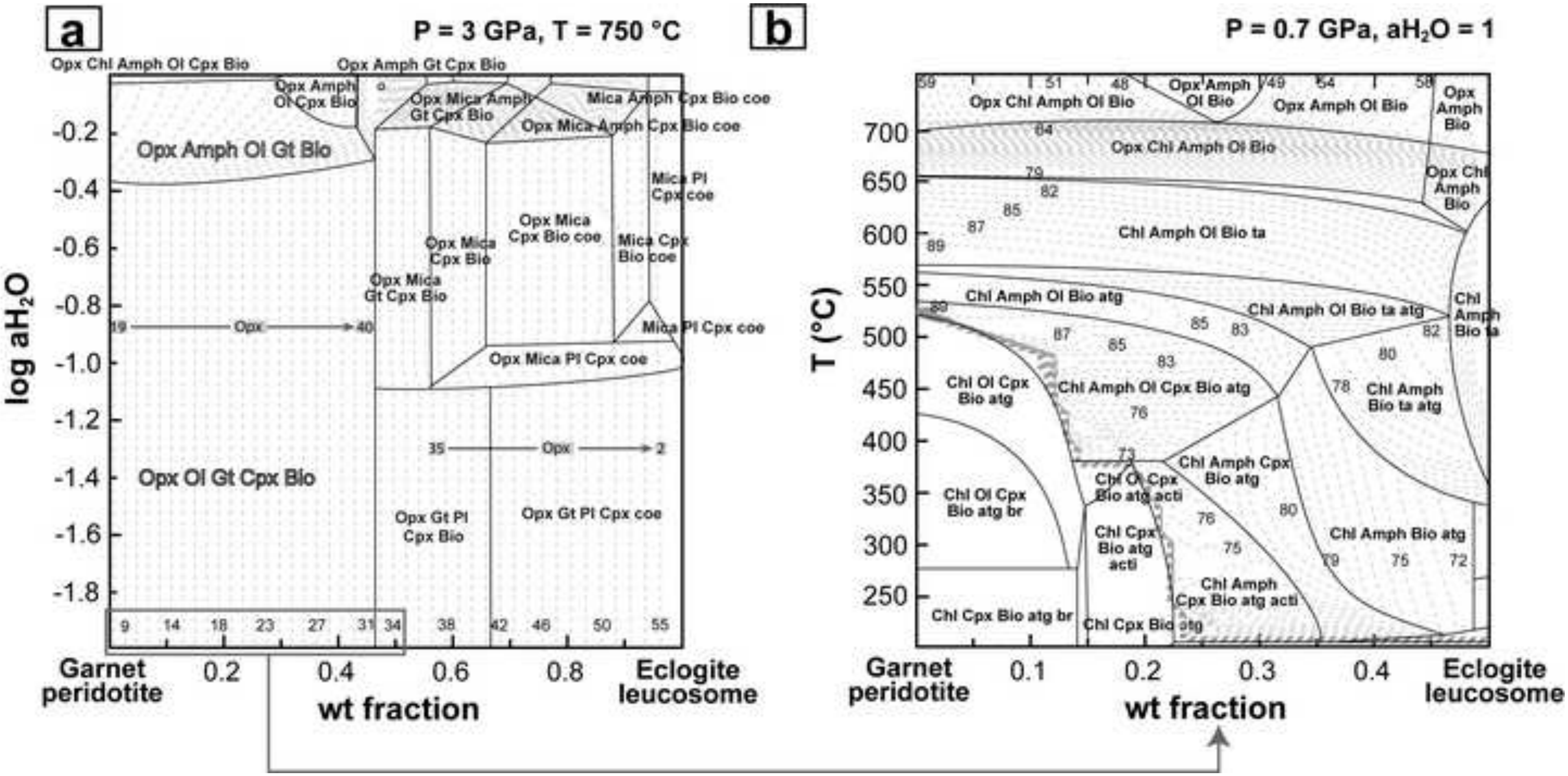

Figure 15
Click here to download high resolution image

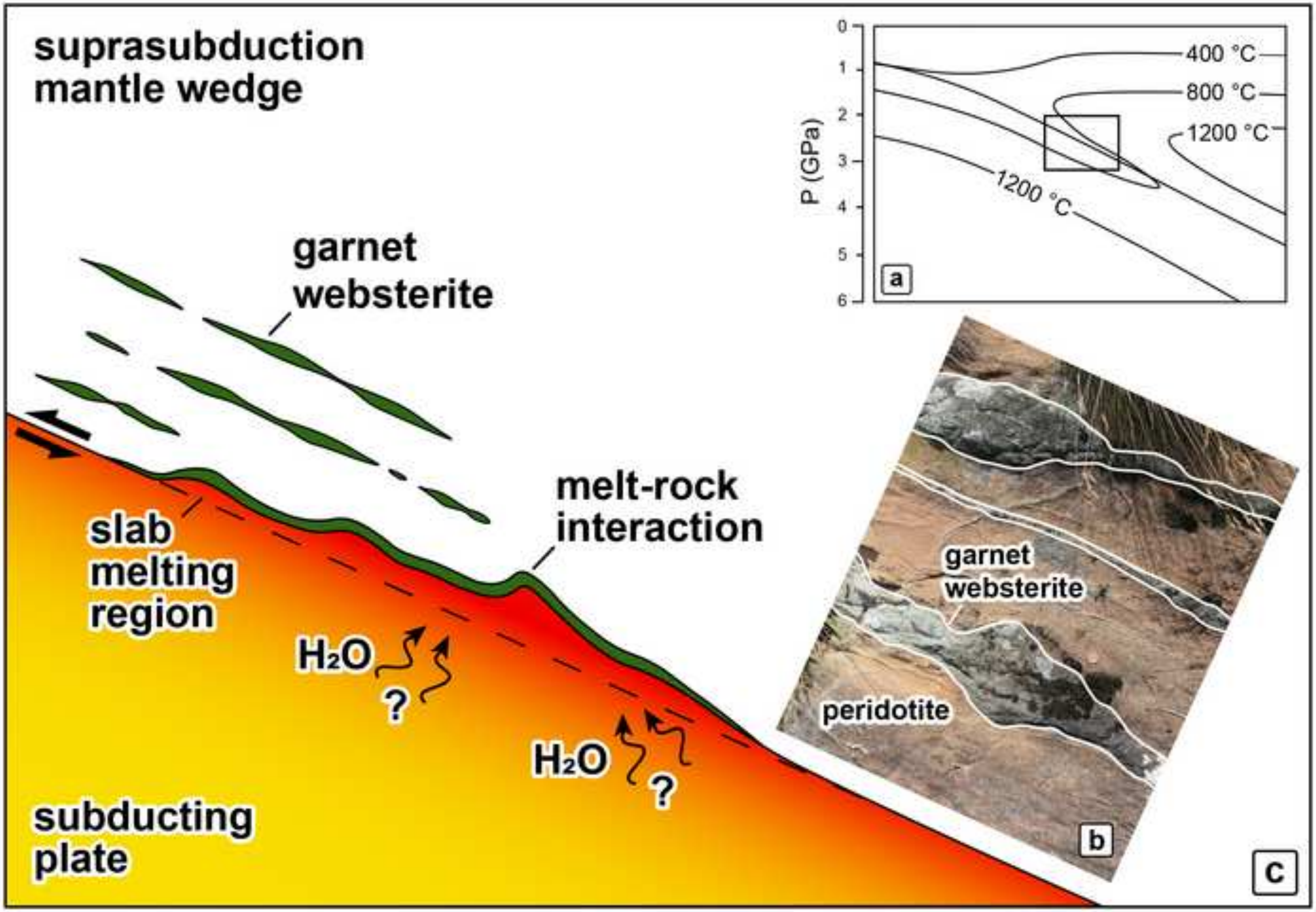

Figure Supp 1

Click here to download high resolution image

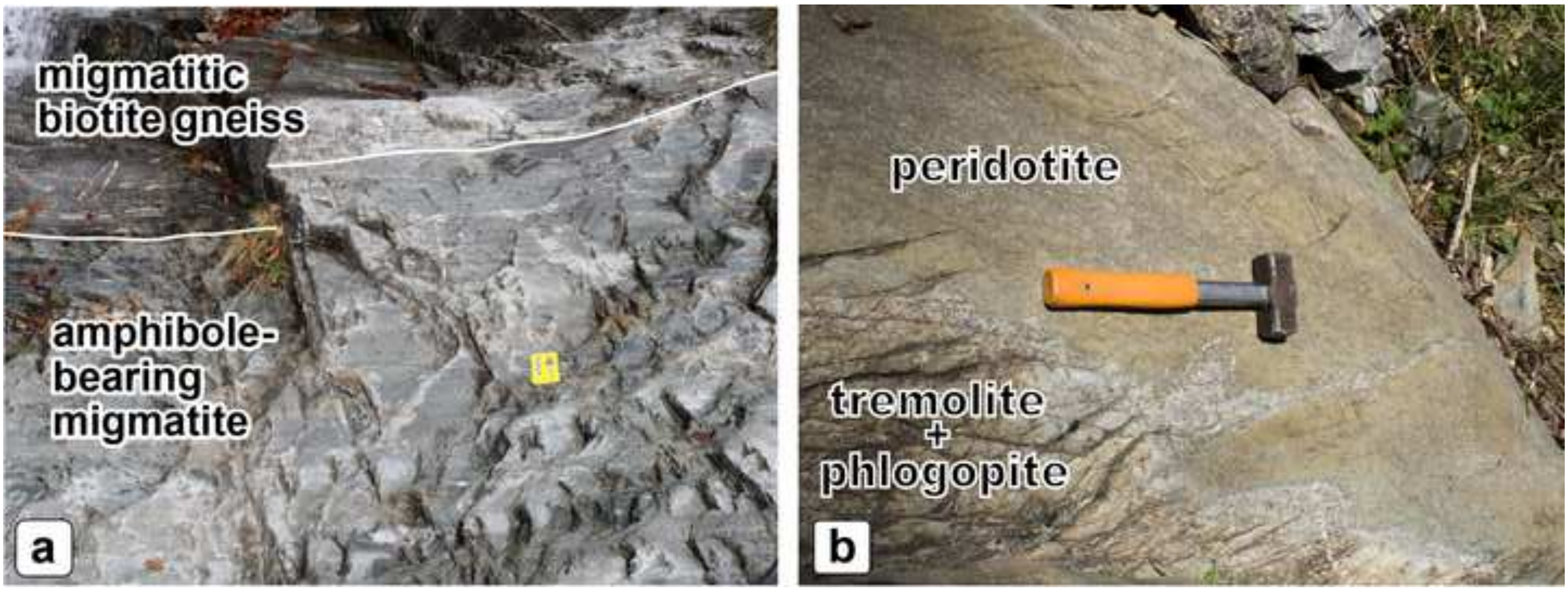

Figure Supp 2
Click here to download high resolution image

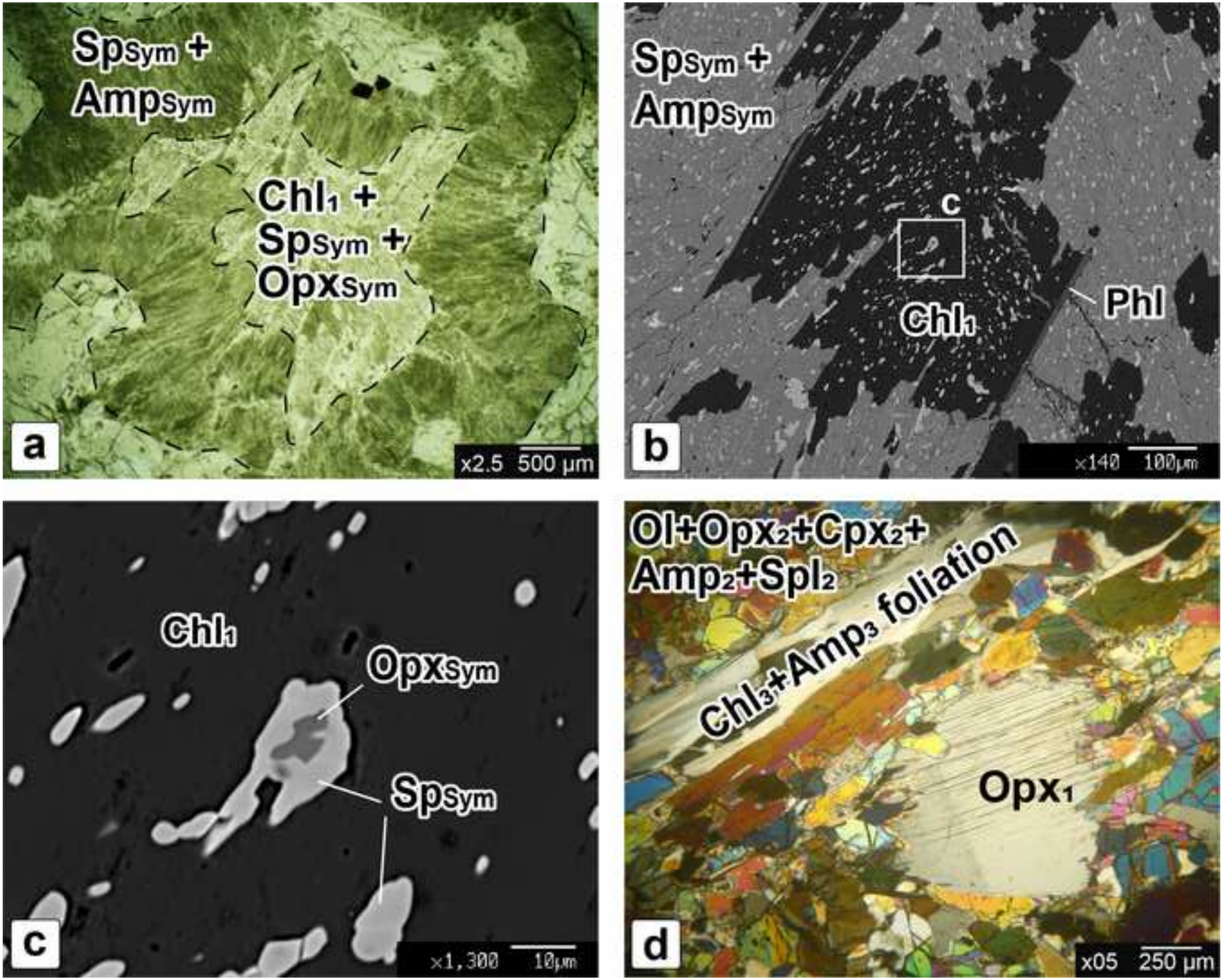

Figure Supp 3

Click here to download high resolution image

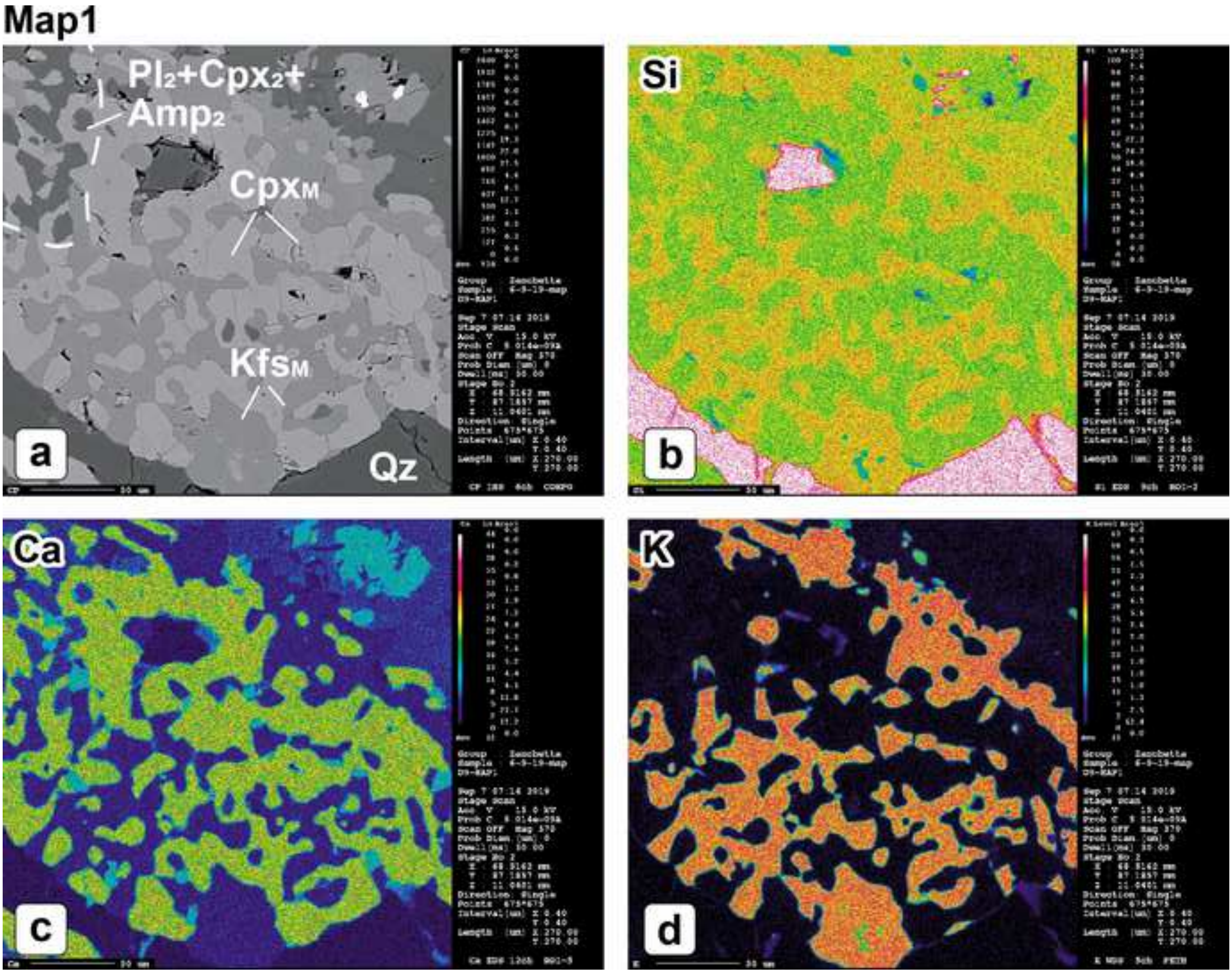

Figure Supp 4

Click here to download high resolution image

Map2

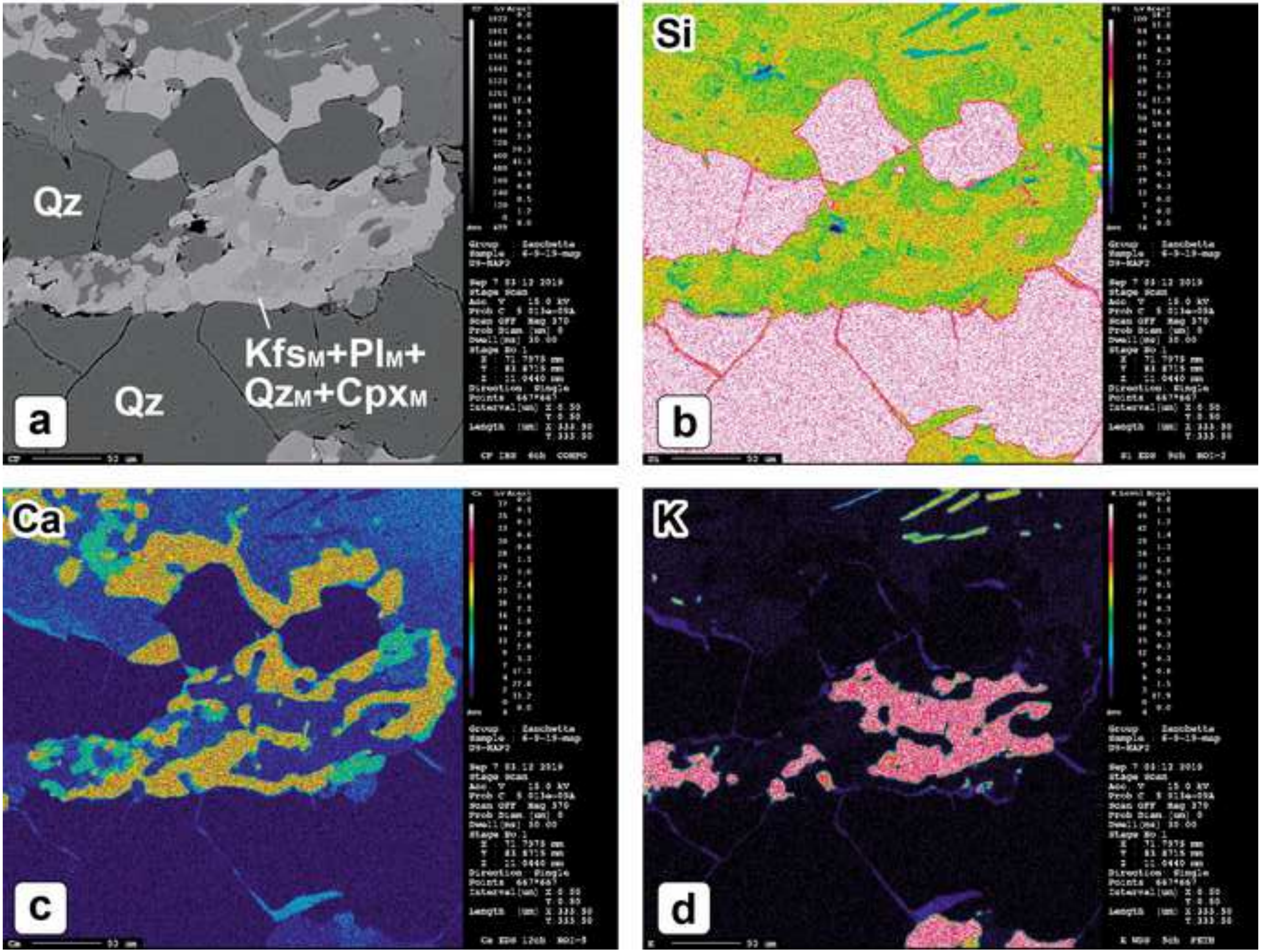

Table 1

Click here to download Table: Table1_new.xlsx

Table 1

Peridotite	HP peak	HP hydration Retrogressed Grt-foliation	HP melt-rock reaction Formation of Grt-websterite	Decompression	LP-(U)HT Sapp-Bdy-Sri*	LP-LT hydration Chl-foliation and Tremolitite
Olivine						
Orthopyroxene			Opx$_{Porph}$ in Chl-peridotite	Opx$_2$	Opx$_{Sym}$	
Clinopyroxene	Cpx$_1$			Cpx$_2$	Cpx$_{Sym}$	
Garnet			Grt in websterite			
Amphibole	Amp$_1$		Amp$_{Porph}$ in Chl-peridotite	Amp$_2$ in Grt-peridotite Hbl in websterite	Amp$_{Sym}$	Amp$_3$ in Chl-peridotite Tr in websterite
Chlorite		Chl$_1$				Chl$_3$
Dolomite						
Phlogopite			Phl$_{Porph}$ in Chl-peridotite			Phl$_3$
Spinel				Sp$_2$	Sp$_{Sym}$	
Talc						
Serpentine						
Calcite						
Brucite						
Eclogite	**HP peak Dol***	**HP hydration Partial melting**		**Decompression**	**LP-(U)HT Sapp-Cor***	**LP-LT hydration**
Clinopyroxene	Omp	Cpx$_M$		Cpx$_2$	Cpx$_{Sym}$	
Quartz		Qz$_M$				
Garnet						
K-feldspar		Kfs$_M$				
Kyanite						
Zoisite						
Allanite						
Rutile						
Amphibole				Amp$_2$		Amp$_3$
Plagioclase		Pl$_M$		Pl$_2$	Pl$_{Sym}$	
Orthopyroxene					Opx$_{Sym}$	
Spinel					Sp$_{Sym}$	
Biotite						

*Tumiati et al. 2018

Table 2
Click here to download Table: Table2_new.xlsx

Table 2

Lithology	Garnet peridotite		Tremolitite	Mafic eclogite	Kyanite eclogite	High-Al_2O_3 eclogite
Sample	B3A	A2C2	DB151	D6	B5	D9
SiO_2	45.66	43.45	55.70	48.96	51.17	51.04
Al_2O_3	2.67	3.05	2.75	15.50	16.11	18.63
FeO†	7.21	8.73	3.48	10.66	5.98	3.23
MgO	36.68	38.58	21.60	9.40	9.85	8.91
CaO	2.16	2.52	12.38	9.57	11.52	11.67
Na_2O	0.14	0.21	0.36	2.01	3.03	3.20
K_2O	0.06	0.01	0.07	0.27	0.26	1.21
TiO_2	0.05	0.12	0.05	1.65	0.54	0.19
P_2O_5	b.d.l.	b.d.l.	0.02	0.10	b.d.l.	b.d.l.
MnO	0.12	0.13	0.07	0.19	0.13	0.06
Cr_2O_3	0.37	0.41	0.62	0.05	0.07	0.12
LOI	3.20	2.40	2.00	0.20	0.40	1.10
CO_2	0.15	b.d.l.	0.10	0.11	0.07	0.26
SO_2	0.06	b.d.l.	b.d.l.	0.10	0.34	0.08
Total	98.53	99.61	99.21	98.77	99.48	99.69
X_{Mg}	0.90	0.90	0.91	0.61	0.75	0.83
Be	1.00	b.d.l.	b.d.l.	b.d.l.	b.d.l.	b.d.l.
Sc	12.0	15.0	33.0	42.0	39.0	18.0
V	50.0	65.0	131	254	161	84.0
Co	91.1	113	37.9	42.1	42.2	24.2
Ni	1975	1862	554	139	121	213
Cu	15.8	15.8	0.80	59.2	359	60.1
Zn	24.0	16.0	5.00	15.0	3.00	9.00
Ga	0.90	b.d.l.	2.70	12.7	10.9	10.9
As	b.d.l.	3.00	b.d.l.	1.80	1.00	0.60
Rb	4.10	0.50	0.30	9.60	5.80	35.8
Sr	5.40	20.7	22.3	39.5	83.8	126
Y	2.50	2.40	3.70	32.3	10.7	4.60
Zr	6.00	10.9	4.50	107	22.4	10.4
Nb	b.d.l.	0.30	0.30	4.10	0.60	0.10
Mo	0.10	b.d.l.	b.d.l.	b.d.l.	b.d.l.	b.d.l.
Cs	0.60	b.d.l.	b.d.l.	0.40	0.40	1.90
Ba	4.00	10.0	b.d.l.	32.0	21.0	189
La	0.50	0.70	1.20	5.70	1.00	1.90
Ce	0.40	1.10	3.50	14.7	2.30	2.80
Pr	0.06	0.14	0.65	2.37	0.40	0.37
Nd	0.40	0.70	3.20	11.4	2.40	1.90
Sm	0.15	0.15	0.95	3.36	1.01	0.42
Eu	0.10	0.12	0.25	1.19	0.42	0.22

Table 3
Click here to download Table: Table3.xlsx

Table 3

Lithology	Grt-peridotite								
Sample	A2C2								
Mineral	Grt C	Grt R	Cpx_1 C	Cpx_1 R	Cpx_2	Cpx_{Sym}	Opx_1	Opx_2	Opx_{Sym}	Ol
SiO_2	42.31	41.84	54.07	54.46	54.96	55.19	56.92	56.28	56.32	39.74
TiO_2	0.08	0.15	0.13	0.13	0.04	0.24	0.10	0.05	0.06	0.01
Al_2O_3	21.69	22.50	1.98	0.94	1.53	1.40	0.80	1.04	1.91	0.00
Cr_2O_3	2.75	1.81	1.34	0.31	0.95	0.03	0.21	0.12	0.01	0.00
FeO†	9.87	10.28	2.46	1.75	1.95	1.84	6.52	6.54	8.43	9.72
MgO	19.02	18.48	16.04	17.57	16.64	17.91	34.95	34.77	33.22	49.88
MnO	0.58	0.57	0.11	0.08	0.08	0.10	0.09	0.13	0.32	0.14
NiO	0.05	b.d.l.	b.d.l.	0.02	0.01	b.d.l.	0.04	0.13	0.05	0.43
CaO	5.69	5.02	23.15	24.53	23.14	24.29	0.22	0.14	0.19	0.01
Na_2O	b.d.l.	0.01	0.81	0.20	0.78	0.06	0.01	0.01	0.03	0.00
K_2O	b.d.l.	0.01	b.d.l.	b.d.l.	b.d.l.	0.01	b.d.l.	b.d.l.	0.01	0.01
Sum	102.04	100.67	100.09	99.99	100.08	101.07	99.86	99.21	100.55	99.94
Si	2.99	2.99	1.97	1.97	1.99	1.98	1.96	1.95	1.95	0.97
Ti	0.00	0.01	0.00	0.00	0.00	0.01	0.00	0.00	0.00	0.00
Al	1.80	1.90	0.08	0.04	0.07	0.06	0.03	0.04	0.08	0.00
Cr	0.15	0.10	0.04	0.01	0.03	0.00	0.01	0.00	0.00	0.00
Fe^{3+}	0.06	0.01	0.00	0.01	0.00	0.00	0.03	0.05	0.03	0.00
Fe^{2+}	0.52	0.61	0.07	0.04	0.06	0.06	0.16	0.14	0.21	0.20
Mg	2.00	1.97	0.87	0.95	0.90	0.96	1.80	1.80	1.71	1.82
Mn	0.03	0.03	0.00	0.00	0.00	0.00	0.00	0.00	0.01	0.00
Ni	0.00	-	-	0.00	0.00	-	0.00	0.00	0.00	0.01
Ca	0.43	0.38	0.90	0.95	0.90	0.93	0.01	0.01	0.01	0.00
Na	-	0.00	0.06	0.01	0.06	0.00	0.00	0.00	0.00	0.00
K	-	0.00	-	-	-	0.00	-	-	0.00	0.00
Cation Sum	8.00	8.00	4.00	4.00	4.00	4.00	4.00	3.99	4.00	3.00
X_{Mg} (=Mg/Mg+Fe^{2+})	0.77	0.76	0.92	0.95	0.94	0.95	0.91	0.93	0.88	0.90

Table 4
Click here to download Table: Table4_new.xlsx

Table 4

Lithology	Grt-peridotite												
Sample	A2C2							B3A					
Mineral	Grt C	Grt R	Cpx_1 C	Cpx_1 R	Opx_1	Amp_1 C	Amp_1 R	Grt C	Grt R	Cpx_1 C	Cpx_1 R	Opx_1	Amp_1 C
Cs	b.d.l.	b.d.l.	0.01	b.d.l.	b.d.l.	0.03	b.d.l.	0.00	b.d.l.	b.d.l.	b.d.l.	b.d.l.	0.02
Rb	0.06	b.d.l.	0.07	b.d.l.	b.d.l.	5.75	4.68	b.d.l.	b.d.l.	b.d.l.	b.d.l.	0.06	1.07
Ba	0.08	0.03	0.44	0.05	b.d.l.	51.8	48.3	0.04	0.01	0.21	0.03	b.d.l.	10.2
K	b.d.l.	b.d.l.	20.9	25.7	12.5	5475	2866	b.d.l.	b.d.l.	39.7	b.d.l.	b.d.l.	1052
Pb	b.d.l.	0.11	1.99	0.30	0.08	26.3	29.4	b.d.l.	b.d.l.	0.08	0.06	b.d.l.	0.93
Th	0.03	0.01	0.01	0.02	b.d.l.	0.03	0.21	0.01	0.01	0.01	b.d.l.	0.01	b.d.l.
U	b.d.l.	b.d.l.	b.d.l.	b.d.l.	b.d.l.	0.06	b.d.l.	b.d.l.	b.d.l.	b.d.l.	b.d.l.	b.d.l.	b.d.l.
Nb	0.02	0.03	0.04	b.d.l.	0.01	1.80	1.61	0.04	0.04	b.d.l.	b.d.l.	0.03	1.81
Ta	b.d.l.	b.d.l.	b.d.l.	b.d.l.	b.d.l.	0.11	0.15	b.d.l.	b.d.l.	b.d.l.	b.d.l.	0.01	0.21
La	b.d.l.	b.d.l.	1.41	1.99	b.d.l.	2.04	1.61	b.d.l.	0.04	0.48	0.62	b.d.l.	0.85
Ce	0.08	0.07	7.29	8.28	0.03	9.25	6.28	0.03	0.05	3.57	3.57	0.03	4.81
Pr	0.07	0.06	1.27	1.53	b.d.l.	1.83	1.70	0.03	0.04	0.93	0.81	b.d.l.	1.17
Sr	0.11	0.19	132	109	0.04	121	143	0.17	0.04	64.0	62.9	0.51	71.7
Nd	0.61	0.70	7.47	8.77	b.d.l.	11.5	8.03	0.61	0.40	4.93	5.26	b.d.l.	6.81
Zr	48.0	50.6	17.1	27.2	0.15	40.5	50.6	62.3	43.7	26.4	24.2	0.37	42.80
Hf	0.45	0.79	1.28	1.24	0.08	2.12	1.52	0.71	0.55	1.21	0.71	b.d.l.	1.60
Sm	0.52	0.81	2.17	2.47	0.06	3.38	4.08	0.80	0.69	2.00	1.79	b.d.l.	3.05
Eu	0.44	0.48	0.57	0.59	b.d.l.	1.11	1.45	0.63	0.46	0.62	0.49	b.d.l.	0.94
Ti	1033	1195	542	676	351	2746	2757	811	726	763	673	382	2522
Gd	1.93	2.52	1.19	1.45	0.08	2.53	6.27	2.18	1.84	1.24	0.79	b.d.l.	2.10
Tb	0.57	0.55	0.20	0.14	b.d.l.	0.43	0.77	0.57	0.40	0.12	0.14	0.04	0.27
Dy	4.16	4.19	0.48	0.41	b.d.l.	1.94	4.24	4.26	3.27	0.58	0.38	0.09	0.80
Y	22.8	23.7	1.56	1.50	0.04	9.32	14.4	26.2	20.7	1.27	1.01	b.d.l.	1.98
Ho	0.90	1.05	0.03	0.05	b.d.l.	0.39	0.45	0.94	0.78	0.02	0.06	b.d.l.	0.14
Er	2.84	2.29	0.18	b.d.l.	b.d.l.	0.86	2.41	2.78	2.25	0.15	0.14	b.d.l.	b.d.l.
Tm	0.35	0.35	0.04	b.d.l.	b.d.l.	0.14	b.d.l.	0.33	0.40	0.01	0.03	0.03	0.03
Yb	2.73	2.61	b.d.l.	0.11	0.11	0.99	b.d.l.	3.10	2.27	0.12	0.09	0.12	b.d.l.
Lu	0.37	0.36	b.d.l.	b.d.l.	0.02	0.16	b.d.l.	0.36	0.37	b.d.l.	b.d.l.	0.01	0.02

Table Supp 1
Click here to download Table: Table S-1_new.xlsx

Table S-1

Lithology					Mafic eclogite			
Sample					D6			
Mineral	Zo C	Zo C	Zo C	Zo R	Zo R	Aln	Aln	Aln
SiO_2	39.04	38.19	38.47	39.00	38.38	35.41	35.34	35.39
TiO_2	0.14	0.12	0.14	0.16	0.12	0.22	0.18	0.11
Al_2O_3	29.65	28.02	28.40	29.10	28.63	21.98	22.22	22.12
Cr_2O_3	b.d.l.	b.d.l.	0.12	b.d.l.	b.d.l.	b.d.l.	b.d.l.	b.d.l.
FeO†	4.19	4.69	4.30	4.09	4.30	8.10	7.79	7.83
MgO	0.44	0.75	0.70	0.65	0.85	1.67	1.76	1.63
MnO	0.02	0.03	0.03	0.02	0.03	0.07	0.01	0.07
NiO	n.a.	n.a.	n.a.	n.a.	n.a.	n.a.	n.a.	n.a.
CaO	22.36	20.38	21.10	21.71	20.69	13.92	14.12	14.19
Na_2O	n.a.	n.a.	n.a.	n.a.	n.a.	n.a.	n.a.	n.a.
K_2O	n.a.	n.a.	n.a.	n.a.	n.a.	n.a.	n.a.	n.a.
SrO	0.55	0.49	0.47	0.13	0.36	b.d.l.	b.d.l.	b.d.l.
La_2O_3	0.21	0.70	0.61	0.55	0.77	3.54	3.37	3.27
Ce_2O_3	0.78	2.15	1.73	1.57	2.16	8.45	8.20	7.99
Pr_2O_3	0.09	0.29	0.28	0.16	0.32	1.22	1.22	1.20
Nd_2O_3	0.70	1.63	1.31	1.22	1.54	4.50	4.41	4.68
Sm_2O_3	0.12	0.42	0.37	0.27	0.31	0.64	0.66	0.69
Eu_2O_3	b.d.l.	b.d.l.	b.d.l.	b.d.l.	0.02	b.d.l.	b.d.l.	b.d.l.
Gd_2O_3	0.20	0.16	0.15	0.12	0.19	0.19	0.26	0.20
Dy_2O_3	b.d.l.	b.d.l.	b.d.l.	b.d.l.	b.d.l.	b.d.l.	b.d.l.	b.d.l.
Y_2O_3	b.d.l.	b.d.l.	b.d.l.	b.d.l.	b.d.l.	b.d.l.	b.d.l.	b.d.l.
PbO	0.03	b.d.l.	0.01	0.01	0.02	b.d.l.	b.d.l.	b.d.l.
ThO_2	0.01	0.14	0.10	0.09	0.12	0.79	0.88	0.76
UO_2	0.07	0.10	0.05	0.03	0.12	0.03	0.00	0.03
Sum	98.59	98.26	98.34	98.86	98.92	100.74	100.43	100.16
Si	4.53	4.56	4.56	4.56	4.54	4.59	4.57	4.59
Ti	0.01	0.01	0.01	0.01	0.01	0.02	0.02	0.01
Al	4.06	3.94	3.96	4.01	3.99	3.36	3.39	3.38
Cr	-	-	0.01	-	-	-	-	-
Fe^{3+}	0.41	0.47	0.43	0.40	0.43	0.88	0.00	0.00
Fe^{2+}	0.00	0.00	0.00	0.00	0.00	0.00	0.84	0.85
Mg	0.08	0.13	0.12	0.11	0.15	0.32	0.34	0.32
Mn	0.00	0.00	0.00	0.00	0.00	0.01	0.00	0.01
Ni	-	-	-	-	-	-	-	-
Ca	2.78	2.61	2.68	2.72	2.62	1.93	1.96	1.97
Na	-	-	-	-	-	-	-	-
K	-	-	-	-	-	-	-	-

*Declaration of Interest Statement

Declaration of interests

- ✓ ☐ The authors declare that they have no known competing financial interests or personal relationships that could have appeared to influence the work reported in this paper.

☐The authors declare the following financial interests/personal relationships which may be considered as potential competing interests:

15th November 2019

Nadia Malaspina